Coastal REsearch And Transportation Education
Tier 1 University Transportation Center
U.S. Department of Transportation

Assessment of Hydrodynamic Properties from Free-Vibration Response of a Prestressed Girder Bridge Model

March 11, 2026

(1) Jorge Loyola-Romero, Graduate Student, Oregon State University, School of Civil and Construction Engineering; ORCID: https://orcid.org/0009-0004-9101-1617; Email: romerolj@oregonstate.edu

(2) Harry Yeh, Ph.D., Professor Emeritus, Oregon State University, School of Civil and Construction Engineering; ORCID: https://orcid.org/0000-0002-0554-3501;Email:harry@oregonstate.edu

(3) Christopher Higgins, Ph.D., P.E., Professor, Oregon State University, School of Civil and Construction Engineering; ORCID: https://orcid.org/0000-0002-2853-3648;Email:chris.higgins@oregonstate.edu

Final Research Report

Prepared for:

Coastal REsearch And Transportation Education

Technical Report Documentation Form

1. Report No.	2. Government Accession No.	3. Recipient's Catalog No.
2301-10	n/a	n/a

4. Title and Subtitle

Assessment of Hydrodynamic Properties from Free-Vibration Response of a Prestressed Girder Bridge Model

5. Report Date

6/01/2026

6. Performing Organization Code

n/a

7. Author(s)

Christopher Higgin 0000-0002-2853-3648; Jorge Loyola-Romero 0009-0004-9101-

8. Performing Organization Report No.

n/a

9. Performing Organization Name and Address

Oregon State University School of Civil Engineering, 5101 Kearney Hall Corvallis, OR US 97331-2302

10. Work Unit No. (TRAIS)

n/a

11. Contract or Grant No.

69A3552348330

12. Sponsoring Agency Name and Address

Office of the Assistant Secretary for Research and Technology
University Transportation Centers Program
Department of Transportation

Final Project Report
06/01/2026

OST-R

15. Supplementary Notes

https://create.engineering.txst.edu/

16. Abstract

An experimental investigation was conducted at Oregon State University's Hinsdale Wave Research Laboratory to quantify hydrodynamic forces acting on bridge structures subjected to dynamic lateral motions under varying submergence conditions. A bridge model mounted on a sliding rail system was subjected to snap-released free-vibration tests under both dry and submerged conditions using two spring configurations to represent different magnitudes of structural stiffness. Dry tests were used to identify intrinsic mechanical properties of the system, including stiffness, damping, and friction. Submerged tests were then analyzed to estimate hydrodynamic added mass and drag coefficients associated with the bridge geometry at differing submergence. Two complementary parameter identification approaches were applied: numerical optimization of the equation of motion using time-history curve fitting, and an instantaneous method that evaluates the governing equation at key response instants. Results show that added mass - the parameter that characterizes the inertial effect - remains approximately constant across excitation amplitudes and is primarily governed by the submerged geometry of the bridge model. In contrast, the effective drag coefficient varies with oscillation amplitude due to nonlinear transient flow behavior. The

17. Key Words	18. Distribution Statement
bridge hydrodynamics; fluid-structure interaction; added mass; hydrodynamic drag; submerged bridge response; SPH modeling;	No Restrictions

19. Security Classification (of this report)	20. Security Classification (of this page)	21. No. of Pages	22. Price
Unclassified	Unclassified	52	n/a

Form **DOT F 1700.7** (8-72) **Reproduction of completed page authorized**

ACKNOWLEDGMENT

This study was funded, partially or entirely, by the U.S. Department of Transportation through the Coastal REsearch and Transportation Education University Transportation Center under Grant Award Number 69A3552348330. The work was conducted at Oregon State University. Any opinions, findings, and conclusions or recommendations expressed are those of the authors and do not necessarily reflect the views of the individuals, companies, or federal agencies.

DISCLAIMER

The contents of this report reflect the views of the authors, who are responsible for the facts and the accuracy of the information presented herein. This document is disseminated under the sponsorship of the U.S. Department of Transportation's University Transportation Centers Program, in the interest of information exchange. The U.S. Government assumes no liability for the contents or use thereof.

ABSTRACT

An experimental investigation was conducted at Oregon State University's Hinsdale Wave Research Laboratory to quantify hydrodynamic forces acting on bridge structures subjected to dynamic lateral motions under varying submergence conditions. A bridge model mounted on a sliding rail system was subjected to snap-released free-vibration tests under both dry and submerged conditions using two spring configurations to represent different magnitudes of structural stiffness. Dry tests were used to identify intrinsic mechanical properties of the system, including stiffness, damping, and friction. Submerged tests were then analyzed to estimate hydrodynamic added mass and drag coefficients associated with the bridge geometry at differing submergence. Two complementary parameter identification approaches were applied: numerical optimization of the equation of motion using time-history curve fitting, and an instantaneous method that evaluates the governing equation at key response instants. Results show that added mass - the parameter that characterizes the inertial effect - remains approximately constant across excitation amplitudes and is primarily governed by the submerged geometry of the bridge model. In contrast, the effective drag coefficient varies with oscillation amplitude due to nonlinear transient flow behavior. The results indicate that inertial hydrodynamic effects dominate bridge response during impulsive loading events and partial submersion allows sloshing of water within the girder lines that attenuates the free-vibration response.

Keywords: bridge hydrodynamics; fluid-structure interaction; added mass; hydrodynamic drag; submerged bridge response; SPH modeling; experimental wave flume testing

Table of Contents

Acknowledgment 2

Disclaimer 3

Abstract 4

Introduction 10

Research Objectives 2

Specific objectives included: 2

Experimental Program 3

Bridge Model 3

Flume Installation 3

Instrumentation 4

Snap-Loading Tests 4

Results 6

Analytical Idealization and Governing Equation of Motion 6

Identification of Mechanical Parameters from Dry Tests 7

Submerged Response 17

Hydrodynamic Model for Submerged Conditions 17

Hydrodynamic Parameter Identification Methods 18

Discussion 34

Added Mass 34

Drag Coefficient 35

Case for constant values of C_d and m_a 36

Fully Submerged Case Analysis of Results 38

Summary and Conclusions 40

Data Availability Statement 42

References 43

List of Figures

Figure 1. Schematic of model cross section, supports, and load cells. 5

Figure 2. Horizontal displacement vs Total lateral force from both springs with maximum initial displacement a) Long Spring, b) Short Spring.. 7

Figure 3. Total horizontal force time history during free-vibration with maximum initial displacement a) Long Spring, b) Short Spring.. 8

Figure 4. Long-spring response cases with no submergence (initial displacement shown). 11

Figure 5. Statistical results of unsubmerged long-spring responses. 12

Figure 6. Short spring responses for no submergence cases... 14

Figure 7. Statistical results of unsubmerged short-spring responses. 16

Figure 8. Cross section of bridge and water height level.. 17

Figure 9. Solutions of added mass and drag coefficient for largest initial displacement of long-spring case with different levels of submergence. 20

Figure 10. Prediction of displacement based on EOM and numerical integration for long-spring case and all initial displacements at water level of H=2.57m... 22

Figure 11. Prediction of displacement based on EOM and numerical integration for long-spring case and all initial displacements at water level of H=2.43m... 23

Figure 12. Prediction of displacement based on EOM and numerical integration for long-spring case and all initial displacements at water level of H=2.36m... 24

Figure 13. Prediction of displacement based on EOM and numerical integration for long-spring case and all initial displacements at water level of H=2.29m... 25

Figure 14. Prediction of displacement based on EOM and numerical integration for long-spring case and all initial displacements at water level of H=2.22m... 26

Figure 15. Prediction of displacement based on EOM and numerical integration for short-spring case and all initial displacements at water depth of H=2.57m.. 28

Figure 16. Prediction of displacement based on EOM and numerical integration for short-spring case and all initial displacements at water depth of H=2.43m.. 28

Figure 17. Prediction of displacement based on EOM and numerical integration for short-spring case and all initial displacements at water depth of H=2.36m.. 29

Figure 18. Prediction of displacement based on EOM and numerical integration for short-spring case and all initial displacements at water depth of H=2.29m.. 30

Figure 19. Prediction of displacement based on EOM and numerical integration for short-spring case and all initial displacements at water depth of H=2.22m. 31
Figure 20. Added mass for all cases with H=2.57m submergence. 35
Figure 21. Drag coefficients for all cases with H=2.57m submergence. 36
Figure 22. Prediction of displacement history based on EOM and numerical integration for short-spring case and all initial displacements with water level of H=2.57m. 38
Figure 23. Prediction of displacement history based on the equation of motion (Eq. 15) and numerical integration for long-spring case and all initial displacements with water level of H=2.57m. 39

List of Tables

Table 1. Summary for free-vibration of long-spring case with no submergence. 11

Table 2. Summary for free-vibration of short-spring case with no submergence. 15

Table 3. Water height levels for snap tests. 17

Table 4. Parameters calculated from Method 1 for largest initial displacement of long-spring case under different submergence level. 21

Table 5. Parameters calculated for long-spring case with water level H=2.57m. 21

Table 6. Parameters calculated from Method 1 for short-spring case with largest initial displacement at different water levels. 27

Table 7. Parameters calculated using CH Instant Method for long-spring case with water level of H=2.57m. 34

Table 8. Parameters calculated using CH Instant Method for short-spring case with water level of H=2.57m. 34

Table 9. Constant values used for long-spring case at fully-submerged conditions with water level of H=2.57m. 37

Table 10. Summary of results for long-spring case at fully submerged water level of H=2.57m. 39

INTRODUCTION

Bridges located along the coast can be subjected to extreme hydraulic loading from storm surge, tsunami inundation, as well as wave and debris impact. These loading events can impose significant hydrodynamic forces on bridge superstructures and have caused major bridge damage and failure during prior coastal events (e.g. Robertson et al. 2007; Guo et al. 2015). Observations following recent tsunami and hurricane events have highlighted the vulnerability of bridge superstructures to hydrodynamic loading, buoyancy effects, and debris impact when water levels rise to the elevation of the bridge girders or deck (Yeh et al., 2013; Istrati and Buckle, 2014).

Hydrodynamic forces acting on submerged or partially submerged structures are typically represented as a combination of inertial and drag components associated with the surrounding fluid. In coastal engineering applications, these forces are often described using the Morison formulation (Morison et al., 1950), which represents the total force as the sum of an inertial term proportional to fluid acceleration and a drag term proportional to the square of the relative velocity between the structure and the fluid (Dean and Dalrymple, 1991). The inertial component is commonly expressed as an added mass, which accounts for the additional fluid that must be accelerated as the structure moves through the surrounding water (Blevins, 1990).

Although these hydrodynamic formulations are widely used for offshore structures, their application to bridge superstructures remains less well established. Bridge cross sections often include multiple girder lines and enclosed cells (from transverse diaphragms) that can entrap water and generate complex fluid-structure interaction effects during dynamic motions. Experimental studies have shown that these interactions can significantly influence the magnitude and distribution of hydrodynamic forces acting on bridges subjected to tsunami and wave loading (Yeh et al., 2013; Istrati and Buckle, 2014).

To improve understanding of these effects, the present study investigates the dynamic response of a bridge superstructure subjected to impulsive lateral motion under varying levels of water submergence. Experiments were conducted using a scaled bridge model installed in the Long Wave Flume at the O. H. Hinsdale Wave Research Laboratory. The bridge model tested follows the geometry used in earlier investigations (Bradner et al. 2010) but expands the experimental matrix to include additional water depths and a wider range of excitation amplitudes. The primary objective was to quantify hydrodynamic added mass and drag forces acting on a bridge superstructure during rapid motion in partially and fully submerged conditions, expanding upon the prior work of Schumacher et. al (2021). These enhancements enable improved characterization of hydrodynamic parameters and provide a robust dataset for model calibration and validation. The data further support development and calibration of numerical models, including Smoothed Particle Hydrodynamics (SPH) simulations of wave–structure interaction.

Research Objectives

The overarching objective of this research was to quantify and model hydrodynamic forces acting on a typical highway bridge structural model subjected to impulsive motion under partially and fully submerged conditions, to determine reliable estimates of added mass and drag coefficients that contribute strongly to fluid-structure interaction.

Specific objectives included:

- Characterize the mechanical behavior of the bridge-support system through dry snap-loading tests to determine baseline stiffness, damping, and friction parameters.
- Measure the dynamic response of the bridge model under varying water depths using controlled snap-loading experiments.
- Estimate hydrodynamic added mass and drag coefficients using time-history analysis and parameter identification methods applied to the measured dynamic response history.
- Evaluate how submergence level and motion amplitude influence hydrodynamic forces and the resulting bridge dynamic response.

EXPERIMENTAL PROGRAM

An experimental program was conducted in the Long Wave Flume of the O. H. Hinsdale Wave Research Laboratory at Oregon State University to investigate the hydrodynamic response of a bridge structure model under varying levels of water submergence. The program utilized a scaled bridge model installed in a large wave flume, allowing controlled testing of structural motion in both dry and submerged conditions.

Bridge Model

The test specimen consisted of a 1:5 scaled bridge superstructure model representing a typical multi-girder prestressed concrete bridge (Bradner et al. 2010). The model is shown in Fig. 1 and included longitudinal girders with Type III cross-sections, composite with a concrete deck, and connected by cross frames, producing internal cavities between girders typical of in-service bridges. The model bridge span was 3.45m, and the width was 1.96m. The total structural mass of the bridge assembly (all moving parts) was approximately 2637 kg, determined by weighing the fabricated components.

The bridge model was mounted to horizontal support beams connected to linear sliding bearing on rails that were supported on fixed steel framing installed within the flume. This system constrained the lateral motion of the bridge to a single degree of freedom while minimizing frictional resistance. Lateral restoring forces were provided by interchangeable springs attached to the sliding support beams. Two spring configurations were used during testing:

1) Long-spring configuration, producing lower stiffness and a longer vibration period.
2) Short-spring configuration, producing higher stiffness and a shorter vibration period.

These two configurations allowed the influence of structural stiffness on the hydrodynamic response to be evaluated in the test program.

Flume Installation

The bridge model and carriage system were installed within the test section of the Hinsdale wave flume. The bridge deck was located 1.6m above the floor of the flume. The bridge was positioned within the central region of the flume to provide sufficient distance from wave reflections both upstream and downstream of the structure during recorded motions. Water depth within the flume was adjusted to produce a range of submergence conditions relative to the bridge cross section, allowing the hydrodynamic response to be examined from dry conditions to full submergence of the structure. The water submergence levels, normalized by the total height of the model (0.280m) were a) z = +0.5 (model under 0.14m of water); b) 0 (even with the top deck surface); c) −0.25; d) −0.50 (model about halfway submerged); e) −0.75.

Instrumentation

The dynamic response of the bridge model during tests was recorded using multiple sensors installed on the carriage and support system. Two horizontal load cells were installed at the spring supports to measure the restoring forces acting on the bridge (See Fig. 1). The forces from these load cells were summed to obtain the total horizontal resisting force acting on the system. Vertical forces were measured from load cells attached to sliding bearings. These can be used to assess uplift and down-drag forces as well as overturning. Bridge displacement was measured using string potentiometers attached between the fixed frame and the moving carriage. These sensors provided high-resolution displacement time histories during each test. Accelerometers were mounted to the bridge structure to record the acceleration response, which was later used to determine velocity and inertial forces for hydrodynamic parameter estimation. All instrumentation was connected to a synchronized data acquisition system that recorded the response during each test at high sampling rates.

Snap-Loading Tests

The testing procedure consisted of snap-release experiments. In each test, the bridge was displaced laterally to a prescribed initial displacement (target of 0.107m for the soft spring case and 0.031m for the stiff spring case) and then suddenly released using a specialty manufactured quick release mechanism. The release of the stored elastic energy in the springs generated an impulsive loading event that caused the bridge to oscillate along the linear rail degree of freedom.

The resulting motion consisted of a free vibration response with gradually decaying amplitude due to friction, structural damping, and hydrodynamic forces when submerged. The displacement, force, and acceleration responses were recorded for each test and used for system identification and hydrodynamic analysis.

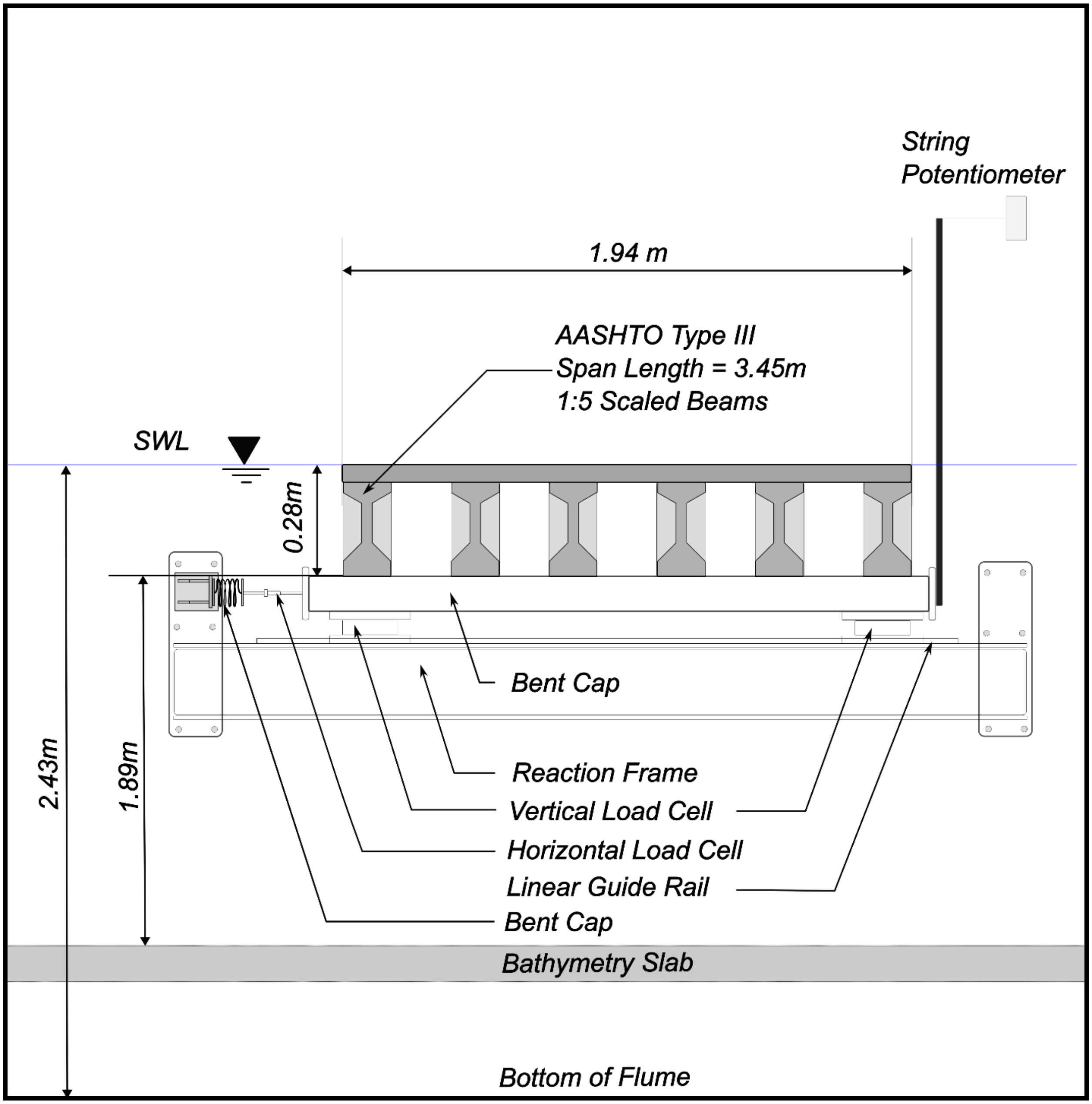

Figure 1. Schematic of model cross section, supports, and load cells.

RESULTS

Analytical Idealization and Governing Equation of Motion

The experimental time-history results were idealized as a single-degree-of-freedom (SDOF) system consisting of mass, linear spring supports, viscous damping, and Coulomb-type friction. The governing equation of motion (EOM) is expressed as:

$$m\ddot{x} + c\dot{x} + kx + sgn(\dot{x})\mu_f mg = 0, \qquad \text{[Eq. 1]}$$

where m is the structural mass, c is the viscous damping coefficient, k is the spring stiffness and $\mu_f mg$ represents the frictional resistance along the rail.

An analytical closed-form solution for the response to an initial displacement was used as the basis for parameter identification, following Markho (1980). The displacement at the n^{th}oscillation is expressed as:

$$x_n = \left[x_0 - x_f(e^{zn} - 1)\coth\left(\frac{z}{4}\right)\right]e^{zn}, \qquad \text{[Eq. 2]}$$

in which,

$$z = \frac{2\pi\zeta}{(1-\zeta^2)^{\frac{1}{2}}} \qquad \text{[Eq. 3]}$$

$$\zeta = \frac{c}{2(km)^{\frac{1}{2}}} \qquad \text{[Eq. 4]}$$

$$\omega_n = \sqrt{\frac{k}{m}} \qquad \text{[Eq. 5]}$$

$$x_f = \frac{\mu_f mg}{k} \qquad \text{[Eq. 6]}$$

Since,

$$\omega_d = \omega_n\sqrt{1-\zeta^2} \qquad \text{[Eq. 7]}$$

and,

$$T = \frac{2\pi}{\omega_d} = \frac{2\pi}{\omega_n\sqrt{1-\zeta^2}} \qquad \text{[Eq. 8]}$$

$$n = \frac{t}{T} \qquad \text{[Eq. 9]}$$

The analytical solution can be written as:

$$a(t) = \left[x_0 - x_f\left(e^{\frac{zt}{T}} - 1\right)\coth\left(\frac{z}{4}\right)\right]e^{-\frac{zt}{T}} \qquad \text{[Eq. 10]}$$

$$a(t) = x_0 e^{-bt} - c_0(e^{bt} - 1)e^{-bt} \qquad \text{[Eq. 11]}$$

where:

$$c_0 = x_f \coth\left(\frac{z}{4}\right) \qquad \text{[Eq. 12]}$$

$$b = \zeta\omega_n \qquad \text{[Eq. 13]}$$

These expressions allow estimation of the damping ratio ζ, friction coefficient μ_f, and stiffness by curve fitting the free-vibration decay obtained from the dry trials (i.e., with no water submergence).

Identification of Mechanical Parameters from Dry Tests

Dry tests served as the baseline for identifying the mechanical properties of the bridge-spring-rail system. Horizontal load cell measurements were summed to represent the total lateral force, accounting for minor asymmetries between the two supports, and the responses for the two spring cases are shown in Fig. 2. Stiffness was computed from dynamic measurements. The dynamic-based estimates showed superior consistency, particularly for the short-spring configuration. The spring stiffnesses were computed based on the maximum force and corresponding extensions. The long spring stiffness was 109 kN/m and the short spring stiffness computed as 404 kN/m.

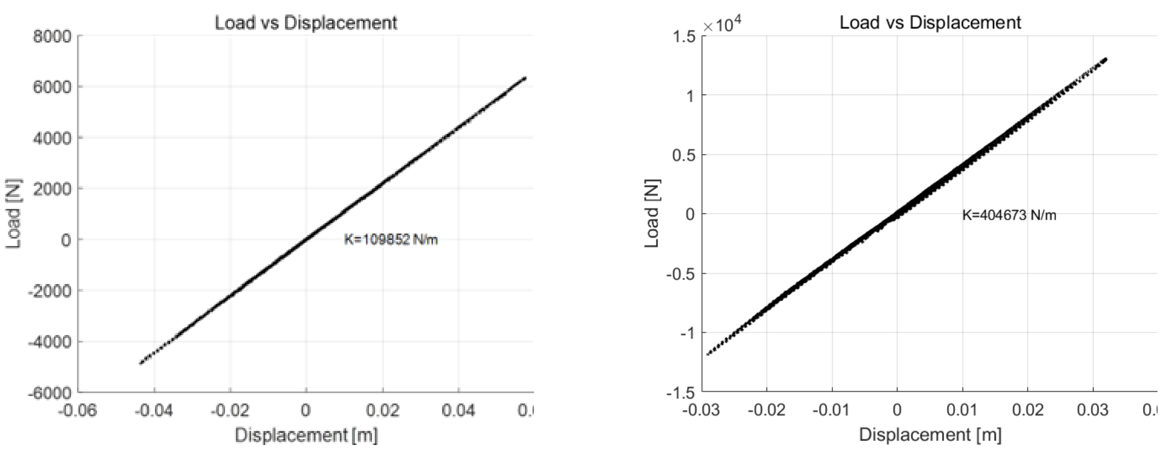

a) b)

Figure 2. Horizontal displacement vs Total lateral force from both springs with maximum initial displacement a) Long Spring, b) Short Spring

Dynamic response analyses were also performed to independently estimate the natural period and stiffness of the system as a means of verification. The relationship between measured loads and corresponding displacements was established using synchronized recordings from both the string potentiometers and the horizontal load cells. The fundamental frequency of the system was identified from the free-vibration response, and the corresponding stiffness was computed using the classical expression for a lightly damped single-degree-of-freedom oscillator:

$$\omega_n = \sqrt{\frac{k}{m}}. \qquad \text{[Eq. 14]}$$

This formulation is appropriate here given the small damping ratios observed in the dry tests. The total system mass of m = 2637 kg was used in this formulation. By combining the measured natural frequency with the known mass, the stiffness k of the support system was determined directly from the expression above. This dynamic-based stiffness estimate provides an important verification and complements the stiffness obtained from the load–displacement characteristics.

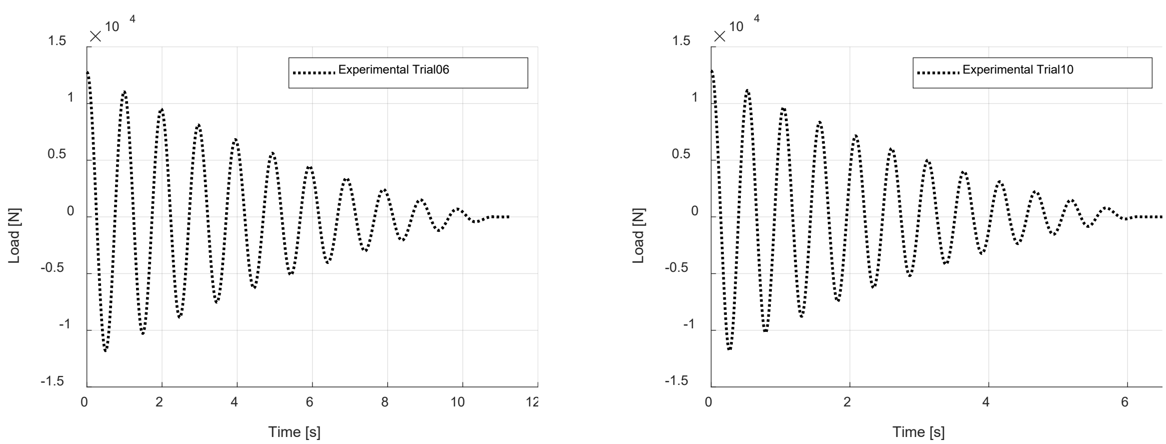

a) b)

Figure 3. Total horizontal force time history during free-vibration with maximum initial displacement a) Long Spring, b) Short Spring

From the free-vibration plots, the natural frequency of the system was identified and used to estimate the corresponding stiffness for each spring configuration. For the long-spring case, the measured period was 0.976 sec. with a corresponding natural frequency of 6.43 rad/sec. For the given mass of the system, the spring stiffness of the long spring is estimated at 109 kN/m. For the short-spring case, the measured period was 0.519 sec. with a corresponding natural frequency of 12.11 rad/sec. For the given mass of the system, the spring stiffness of the short spring is estimated at 404 kN/m.

With the stiffness values established, displacement time histories were computed by dividing the measured horizontal load-cell forces by the appropriate stiffness. These displacement responses were then used for exponential-decay curve fitting to estimate damping and friction parameters for each trial. Displacement measurements from the string potentiometers were used to verify the load-cell-derived displacement responses and ensured consistency of the extracted system properties.

Using the calibrated parameters from curve fitting, the full equation of motion was solved numerically using a fourth-order Runge–Kutta method. This numerical integration accounts for inertial effects, viscous damping, and Coulomb friction as defined in the governing SDOF moel (Eq. 1).

For the long-spring configuration under dry conditions (no submergence), the system response corresponding to different initial displacements are presented below in Figure 4.

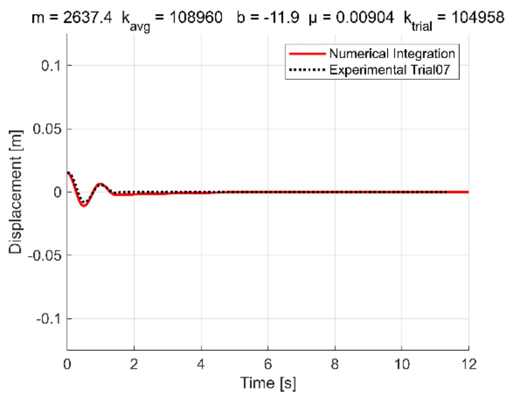

Initial Displacement = 0.0151 m.

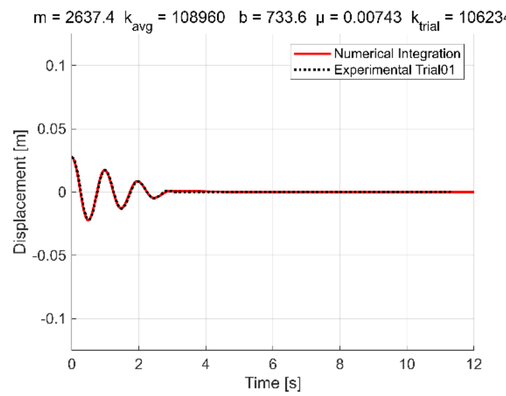

Initial Displacement = 0.0225 m.

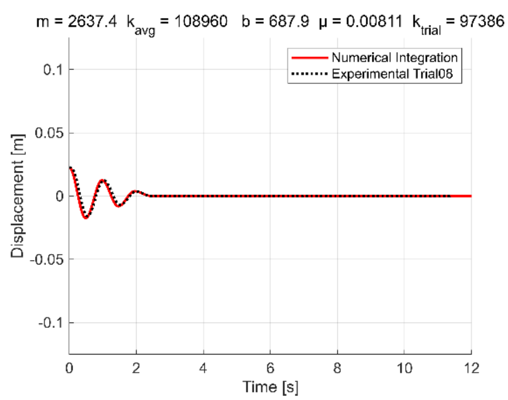

Initial Displacement = 0.0275 m.

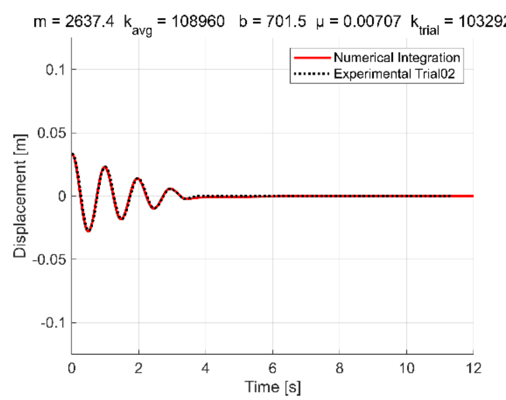

Initial Displacement = 0.0334 m.

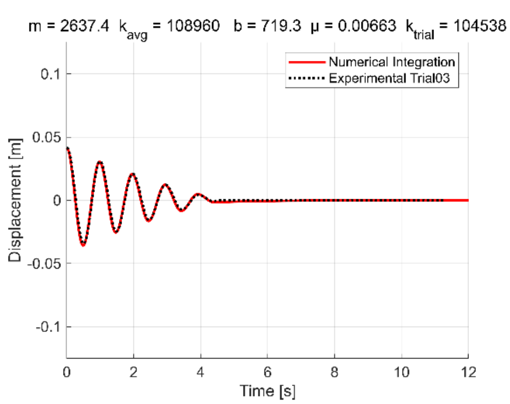

Initial Displacement = 0.0416 m.

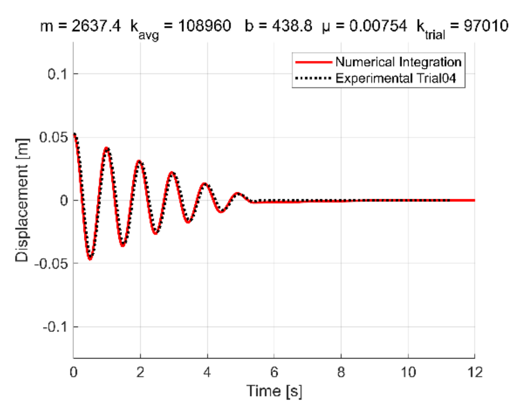

Initial Displacement = 0.0524 m.

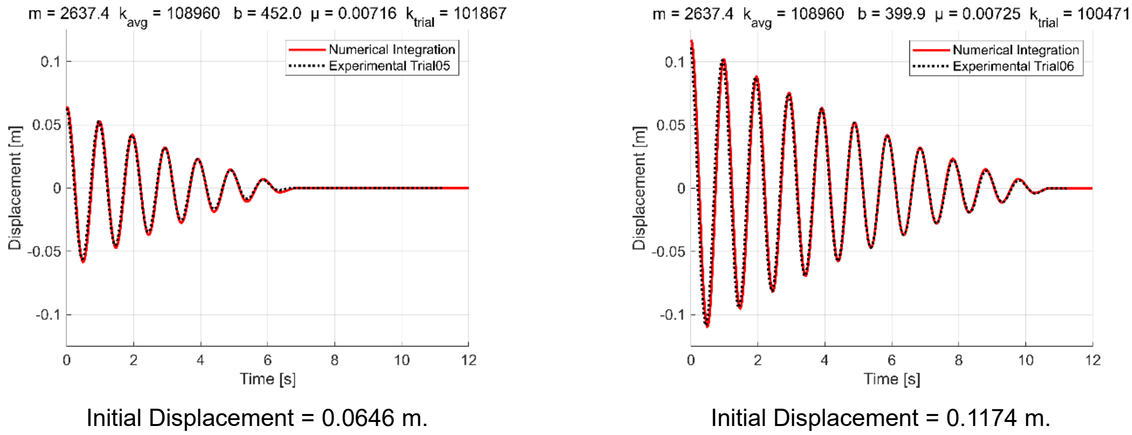

Figure 4. Long-spring response cases with no submergence (initial displacement shown).

A summary of the damping ratio, friction coefficient, and initial displacement for the long-spring configuration under dry, no-submergence conditions is provided in Table 1. These values represent the calibrated system parameters obtained from curve-fitting the free-vibration decay and serve as the baseline mechanical properties for subsequent submerged-condition analyses.

Table 1. Summary for free-vibration of long-spring case with no submergence.

Initial Displacement [m]	Initial Load [N]	ζ [-]	Damping	Friction Coeff [-]	Stiffness [kN/m]
0.0225	2454	0.0202	687	0.00810	109177
0.0275	2994	0.0216	734	0.00741	109610
0.0334	3641	0.0206	701	0.00705	109085
0.0416	4530	0.0211	719	0.00662	109276
0.0524	5713	0.0129	439	0.00752	109609
0.0646	7034	0.0133	452	0.00714	109788
0.1174	12796	0.0118	400	0.00723	110601
Average		0.0174	590	0.00729	109592

The average values of the damping, stiffness, and friction coefficient for the long-spring configuration are shown in Table 1 and Figure 5. These averaged parameters provide a representative characterization of the system behavior and are used as reference values for comparison with the submerged test cases.

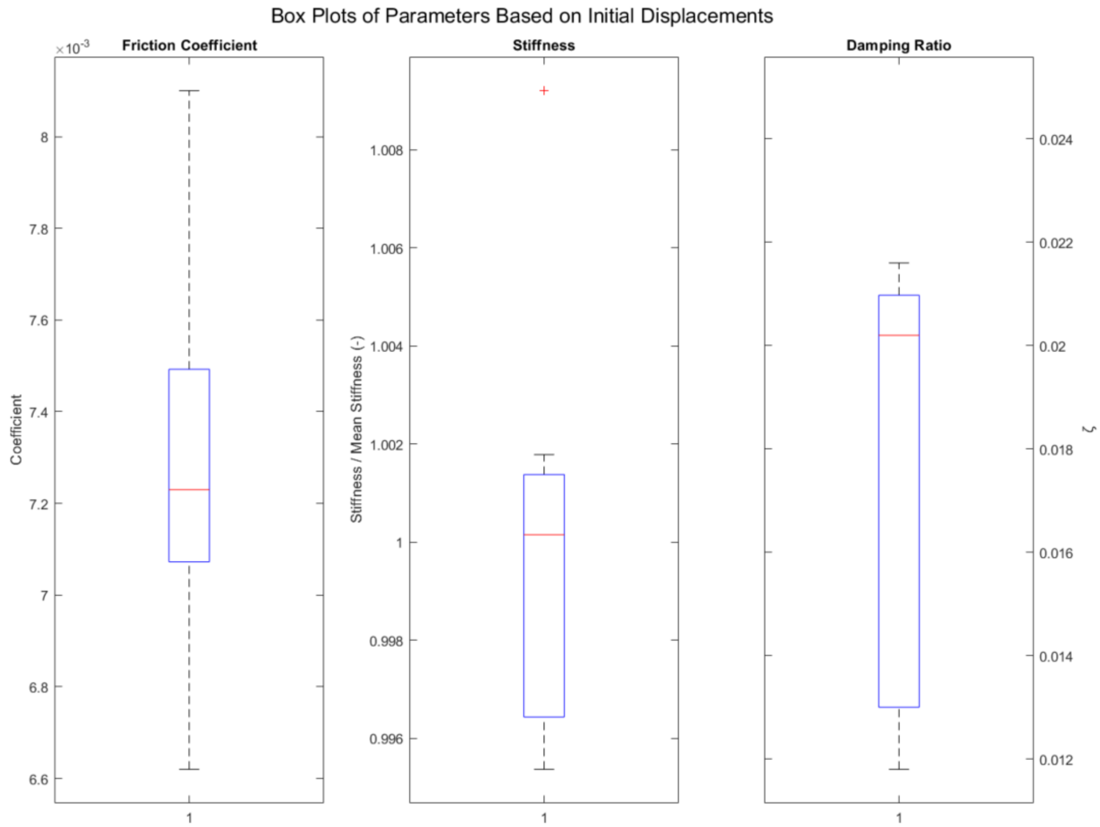

Figure 5. Statistical results of unsubmerged long-spring responses.

For the short-spring configuration under dry conditions, the system exhibited a series of free-vibration responses at various initial displacements. These results are shown in Figure 6 and illustrate greater sensitivity of the short-spring system to small variations in initial excitation.

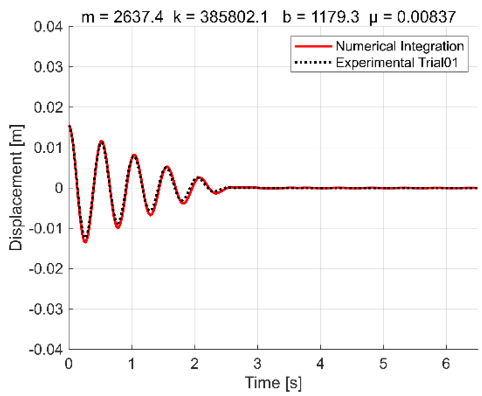

Initial Displacement = 0.0155 m.

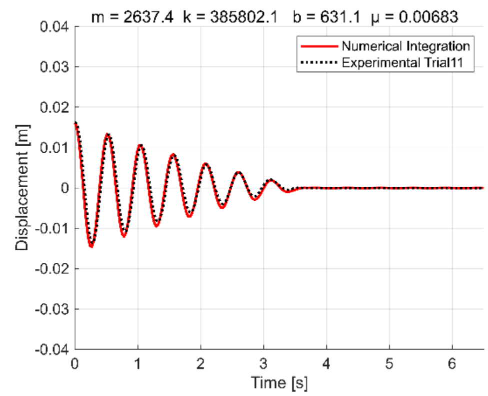

Initial Displacement = 0.0156 m.

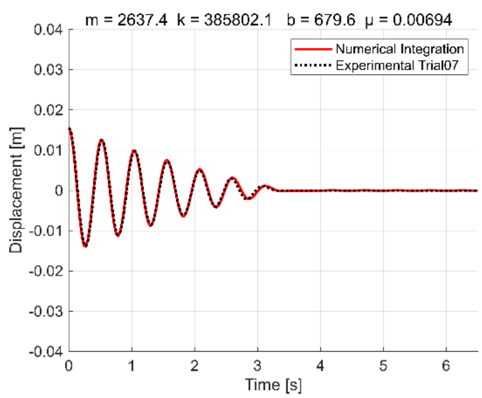

Initial Displacement = 0.0161 m.

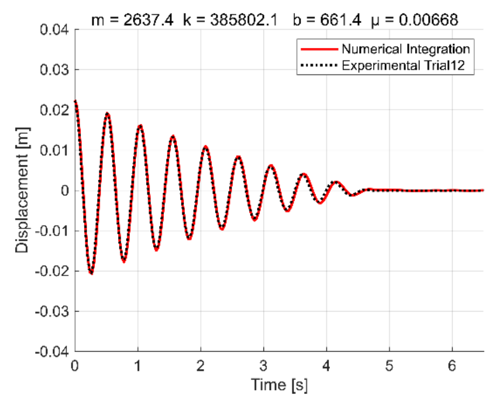

Initial Displacement = 0.0225 m.

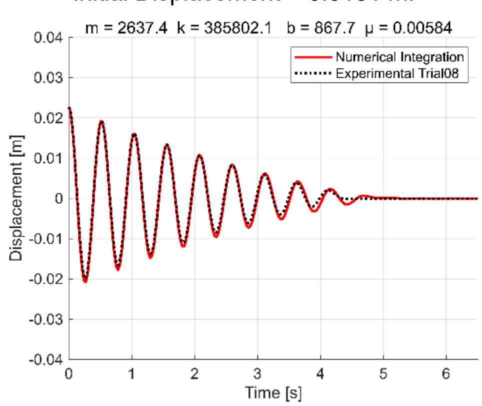

Initial Displacement = 0.0227 m.

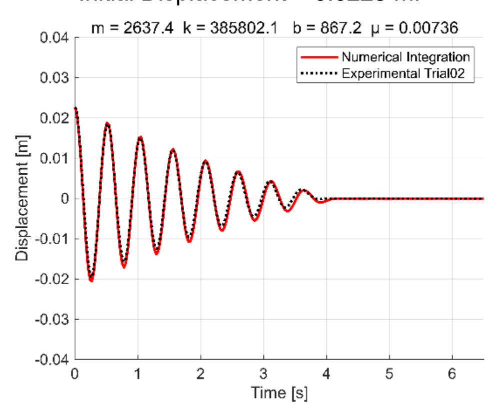

Initial Displacement = 0.0227 m.

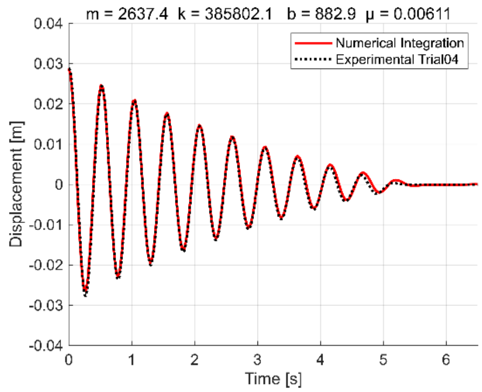

Initial Displacement = 0.0288 m.

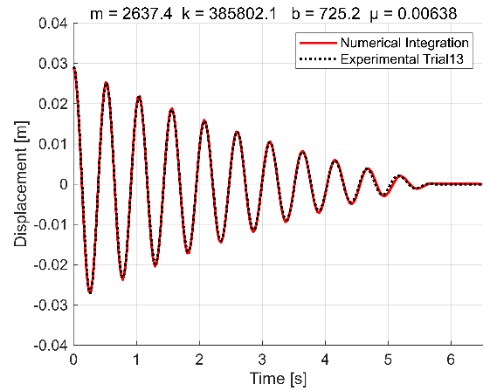

Initial Displacement = 0.291 m.

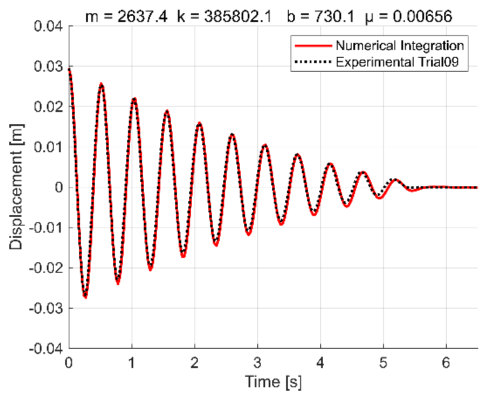

Initial Displacement = 0.0295 m.

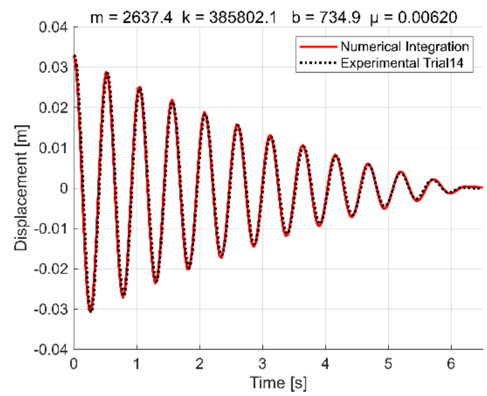

Initial Displacement = 0.329 m.

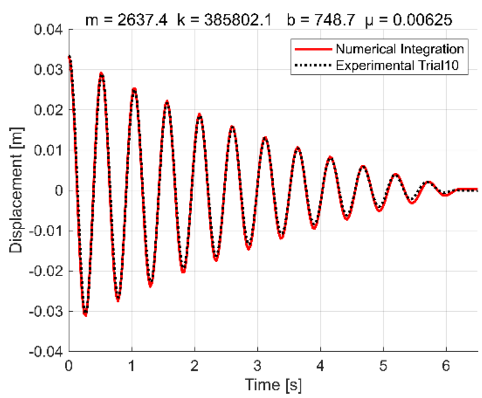

Initial Displacement = 0.0330 m.

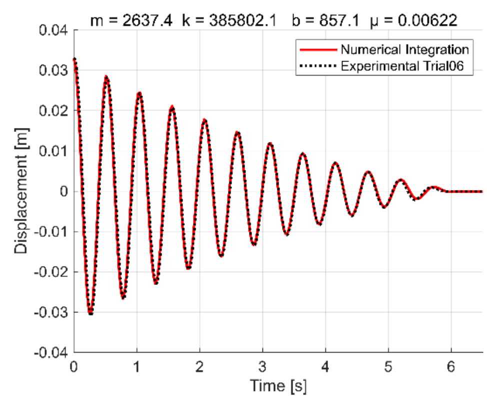

Initial Displacement = 0.334 m.

Figure 6. Short spring responses for no submergence cases.

A summary of the damping ratio, friction coefficient, and initial displacement for the short-spring configuration under dry, no-submergence conditions is presented in Table 2 and Figure 7. For these trials, the system response was more accurately represented when using the stiffness values obtained from the dynamic free-vibration analysis rather than those derived from static load–displacement measurements, indicating improved consistency in the dynamic-based stiffness characterization.

Table 2. Summary for free-vibration of short-spring case with no submergence.

Initial Displacement [m]	Initial Load [N]	ζ [-]	Damping	Friction Coeff [-]	Stiffness [kN/m]
0.0149	5971	0.0106	680	0.00693	401444
0.0150	6002	0.0184	1179	0.00836	400152
0.0156	6223	0.0098	629	0.00672	398343
0.0216	8666	0.0103	662	0.00669	401956
0.0217	8764	0.0152	974	0.00521	403422
0.0218	8744	0.0166	1061	0.00645	401853
0.0276	11111	0.0131	839	0.00666	403259
0.0279	11241	0.0118	756	0.00618	402509
0.0284	11395	0.0114	730	0.00655	401390
0.0314	12691	0.0115	735	0.00625	403921
0.0315	12713	0.0134	857	0.00620	403720
0.0320	12893	0.0117	748	0.00633	402464
Average		0.0128	821	0.00654	402036

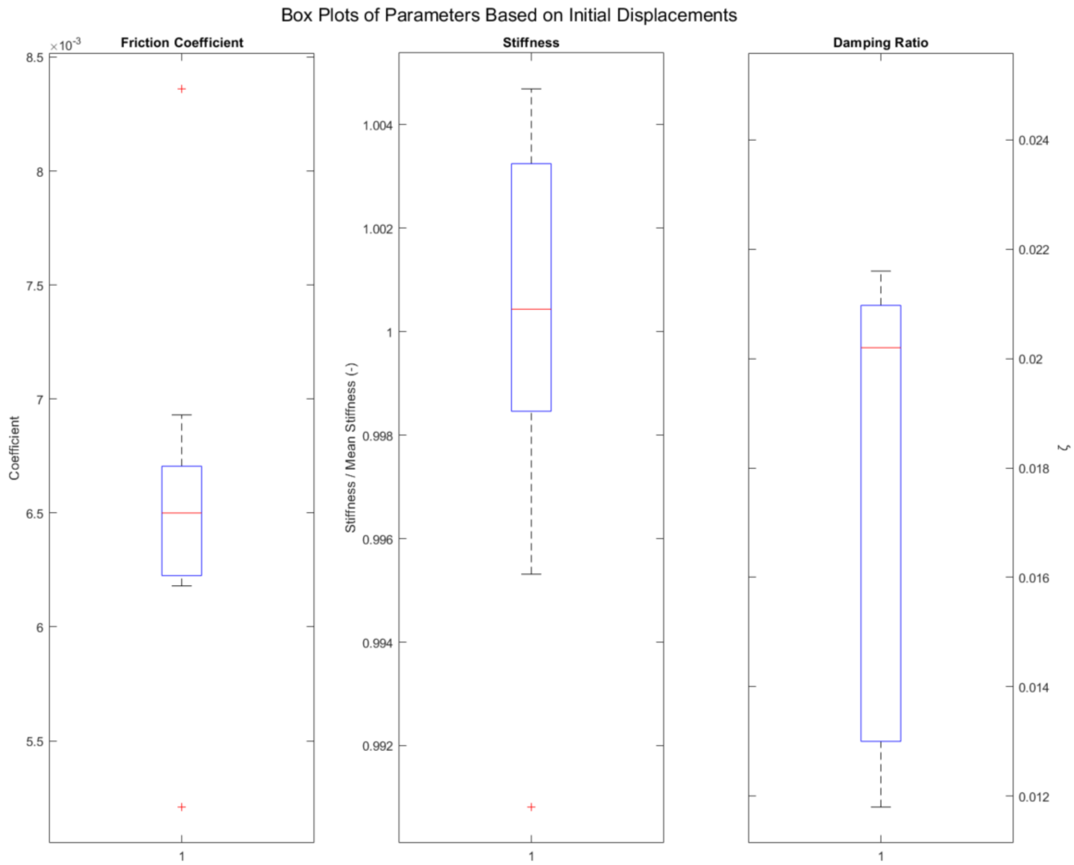

Figure 7. Statistical results of unsubmerged short-spring responses.

Submerged Response

With the dry-condition behavior characterized, including the intrinsic damping and friction for both spring configurations, attention was then directed to the submerged cases. By analyzing the bridge response under varying water depths, the influence of hydrodynamic effects-specifically added mass and drag-were quantified. The sequence of water-level conditions evaluated in the submerged testing program is summarized in Table 3 and illustrated schematically in Figure 8, providing the basis for assessing how increasing submergence alters the dynamic response of the system.

Table 3. Water height levels for snap tests.

Test	Water Depth (m)	Comment
1	1.63	Dry
2	2.22	Min. Height
3	2.29	Mid. Height 1
4	2.36	Mid. Height 2
5	2.43	Deck level
6	2.57	Max. Height

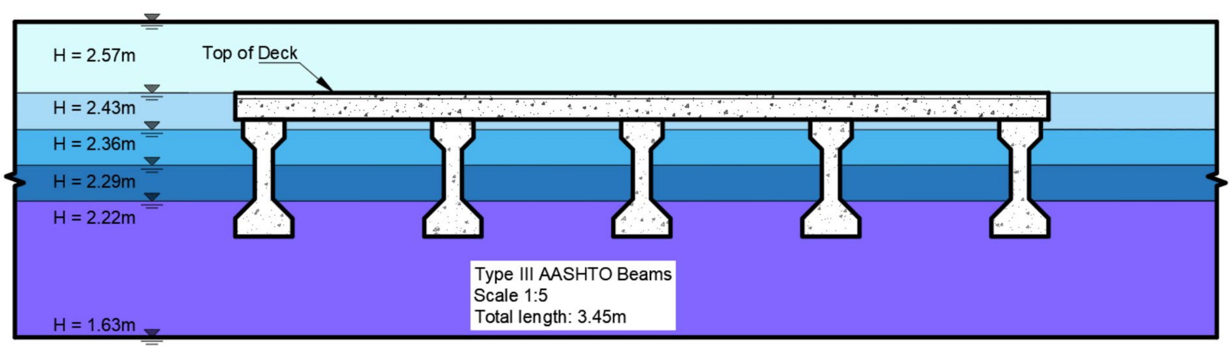

Figure 8. Cross section of bridge and water height level.

Hydrodynamic Model for Submerged Conditions

The equation of motion (Eq. 1) was expanded to incorporate the hydrodynamic effects associated with water submergence. Two additional terms were introduced to account for added mass and drag forces acting on the bridge during free-vibration, and a buoyancy correction was applied to adjust the effective frictional resistance along the rails due to reduced normal force on the linear bearings. The modified governing equation includes contributions from structural inertia, added mass, viscous damping, Coulomb friction, and hydrodynamic drag, providing a comprehensive representation of the system under submerged conditions.

$$m\ddot{x} + c\dot{x} + kx + sign(\dot{x})\mu_f(mg - \forall\rho_w g) + m_a\ddot{x} + \frac{1}{2}C_d\,\rho_w\,A\dot{x}|\dot{x}| = 0 \qquad \text{[Eq. 15]}$$

where $\forall$ is the volume of the structure submerged (Buoyancy force), ρ_w is the mass density of water, m_a is the added mass, C_d is the drag coefficient, and A is the transverse cross-sectional area of the bridge.

In this formulation, the submerged volume of the structure determines the buoyancy force, the water density governs the magnitude of hydrodynamic effects, the added mass term represents the inertia of the entrained water moving with the structure, and the drag coefficient defines the resistance induced by relative fluid motion. The transverse area of the bridge is used to scale the drag force contribution. Together, these terms characterize the fluid–structure interaction effects introduced by submergence.

Hydrodynamic Parameter Identification Methods

The influence of added mass and drag was quantified using two approaches. The first approach employed numerical optimization and curve fitting to match the measured displacement response with predictions from the modified equation of motion. The second method, proposed here, estimates the added mass and drag coefficients by evaluating the equation of motion at specific key instances in the response history. Together, these two methods provide independent means of extracting hydrodynamic parameters from the experimental data.

Method 1 - Optimization and Curve Fitting

This method combines the analytical free-vibration formulation with numerical optimization to estimate the added mass and drag coefficients. MATLAB's *fminsearch* algorithm was used to minimize the error between the measured displacement time series and the numerically integrated response of the modified equation of motion. Starting from initial trials for the added mass and drag coefficients, the algorithm iteratively adjusts these parameters, recomputes the numerical solution using a fourth-order Runge-Kutta method, and evaluates the resulting residual error. Convergence is achieved when the RMS difference between the measured and predicted responses is minimized, and the corresponding parameter values are accepted as the solution for that trial.

The optimized values of the added mass and drag coefficients obtained for the largest initial displacement in each submergence case are summarized in Figure 9. These results illustrate the dependence of the hydrodynamic parameters on the level of submergence, with increasing water depth generally producing higher added mass and drag values due to greater fluid–structure interaction.

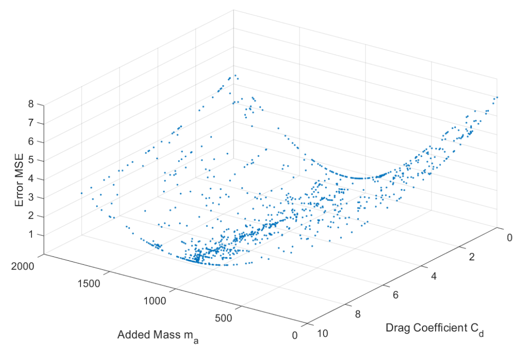

Optimization Results

$m_a = 1271.37$ kg

$C_d = 8.085$

Full Submergence H= 2.57 m.

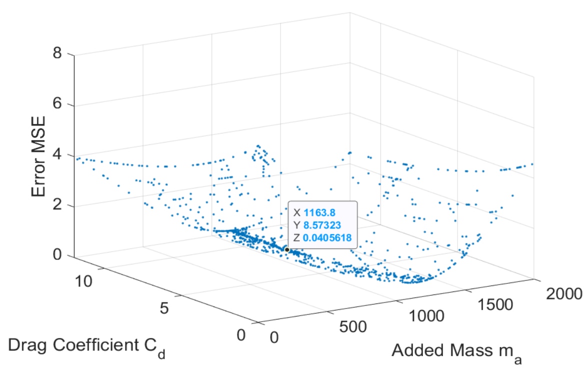

Optimization Results

$m_a = 1169.04$ kg

$C_d = 8.589$

Full Submergence H= 2.43 m.

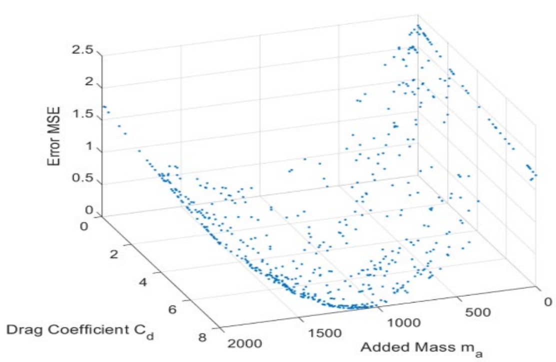

Optimization Results

$m_a = 1079.4$ kg

$C_d = 7.99$

Partial Submergence H= 2.36 m.

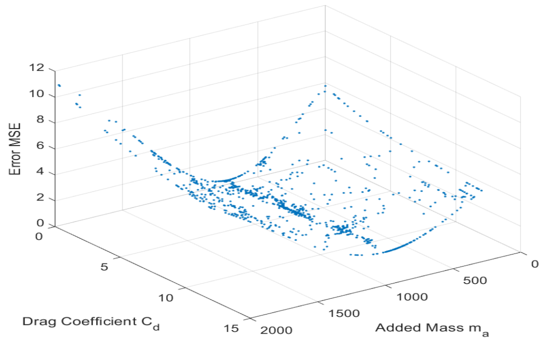

Optimization Results

m_a = 717.10 kg

C_d = 3.925

Partial Submergence H=2.29 m.

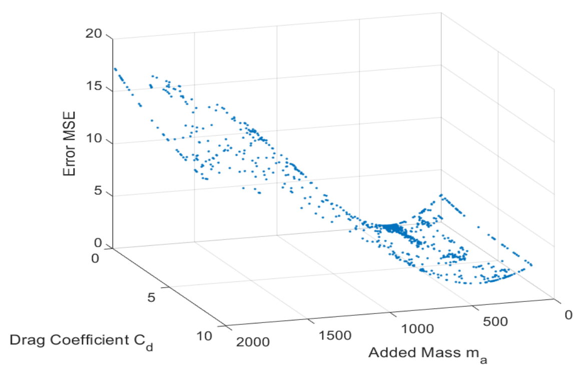

Optimization Results

m_a = 322.9 kg

C_d = 1.467

Partial Submergence H=2.22 m.

Figure 9. Solutions of added mass and drag coefficient for largest initial displacement of long-spring case with different levels of submergence.

Using the optimized parameter values shown in Figure 9, numerical predictions of the displacement response were generated for each initial displacement level across all submergence conditions. These predictions are presented in Figure 10-14 and demonstrate the ability of the modified equation of motion to capture the amplitude decay and oscillatory behavior of the submerged system under varying hydrodynamic conditions.

Table 4. Parameters calculated from Method 1 for largest initial displacement of long-spring case under different submergence level.

Submergence H [m]	m_a [kg]	C_d [-]	Mass of water in cells [kg]	Initial Disp. [m]
2.22	322.9	1.47	300	0.108
2.29	717.8	3.93	669	0.108
2.36	1079.4	8.00	1015	0.108
2.43	1169.0	8.59	1104	0.108
2.57	1271.4	8.09	1104	0.108

The optimization procedure was applied to all initial displacement levels for the fully submerged condition, H = 2.57m, resulting in a complete set of added mass and drag coefficients for every trial. These values are shown in Table 5. As expected, the coefficients exhibit variation with initial energy: the drag coefficient shows a strong dependence on displacement amplitude, while the added mass remains comparatively consistent, reflecting its geometric and submergence-driven nature.

Table 5. Parameters calculated for long-spring case with water level H=2.57m.

Initial Displacement [m]	Potential Energy [kN-m] [kJ]	Added Mass [kg]	Drag Coefficient [-]
0.018	17.9	1196	44.86
0.026	37.6	1198	27.09
0.030	49.2	1419	30.73
0.032	55.1	1111	23.92
0.036	70.3	1819	30.76
0.044	105.6	1206	15.56
0.055	167.1	1196	12.34
0.064	223.3	953	6.87
0.109	644.3	1271	8.09

The drag coefficient trends reveal that increasing initial displacement generally produced lower drag coefficients, suggesting reduced hydrodynamic resistance at higher oscillation amplitudes. This behavior is consistent with nonlinear flow effects, where separated flow patterns exert proportionally smaller drag at larger velocities. In contrast, the added mass does not exhibit a clearly increasing trend with displacement, indicating that inertial fluid forces are governed primarily by submergence geometry rather than excitation amplitude.

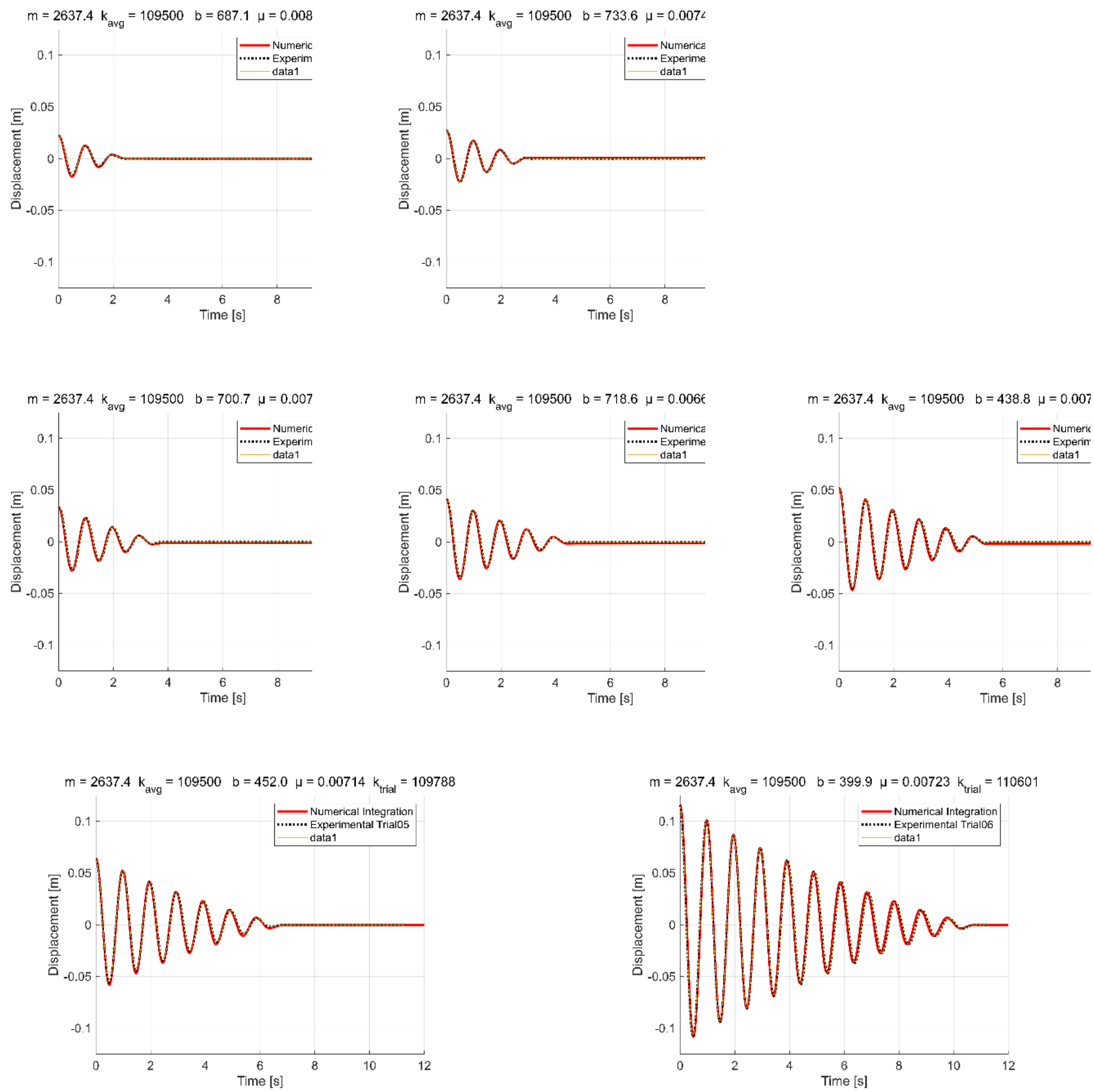

Figure 10. Prediction of displacement based on EOM and numerical integration for long-spring case and all initial displacements at water level of H=2.57m.

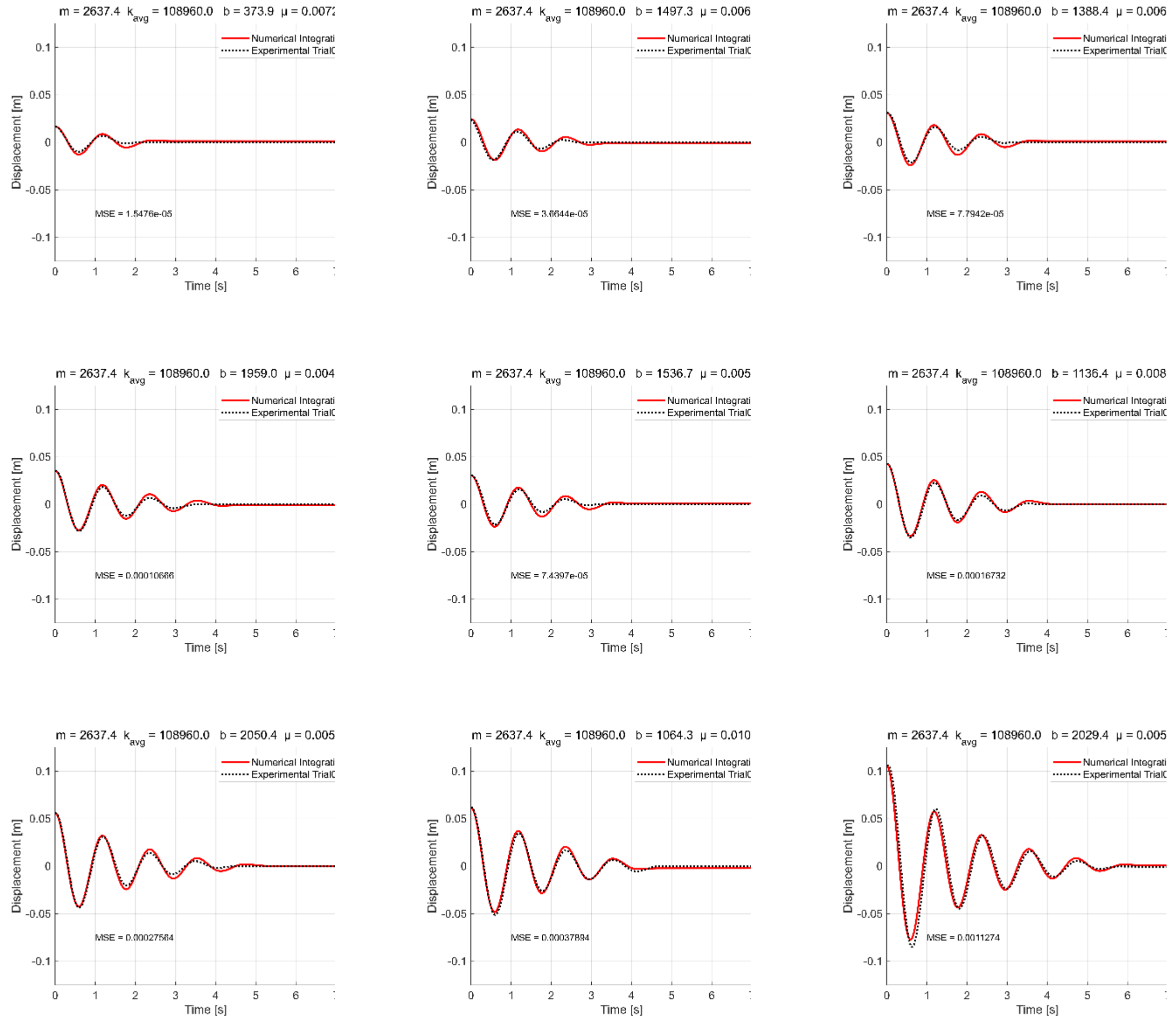

Figure 11. Prediction of displacement based on EOM and numerical integration for long-spring case and all initial displacements at water level of H=2.43m.

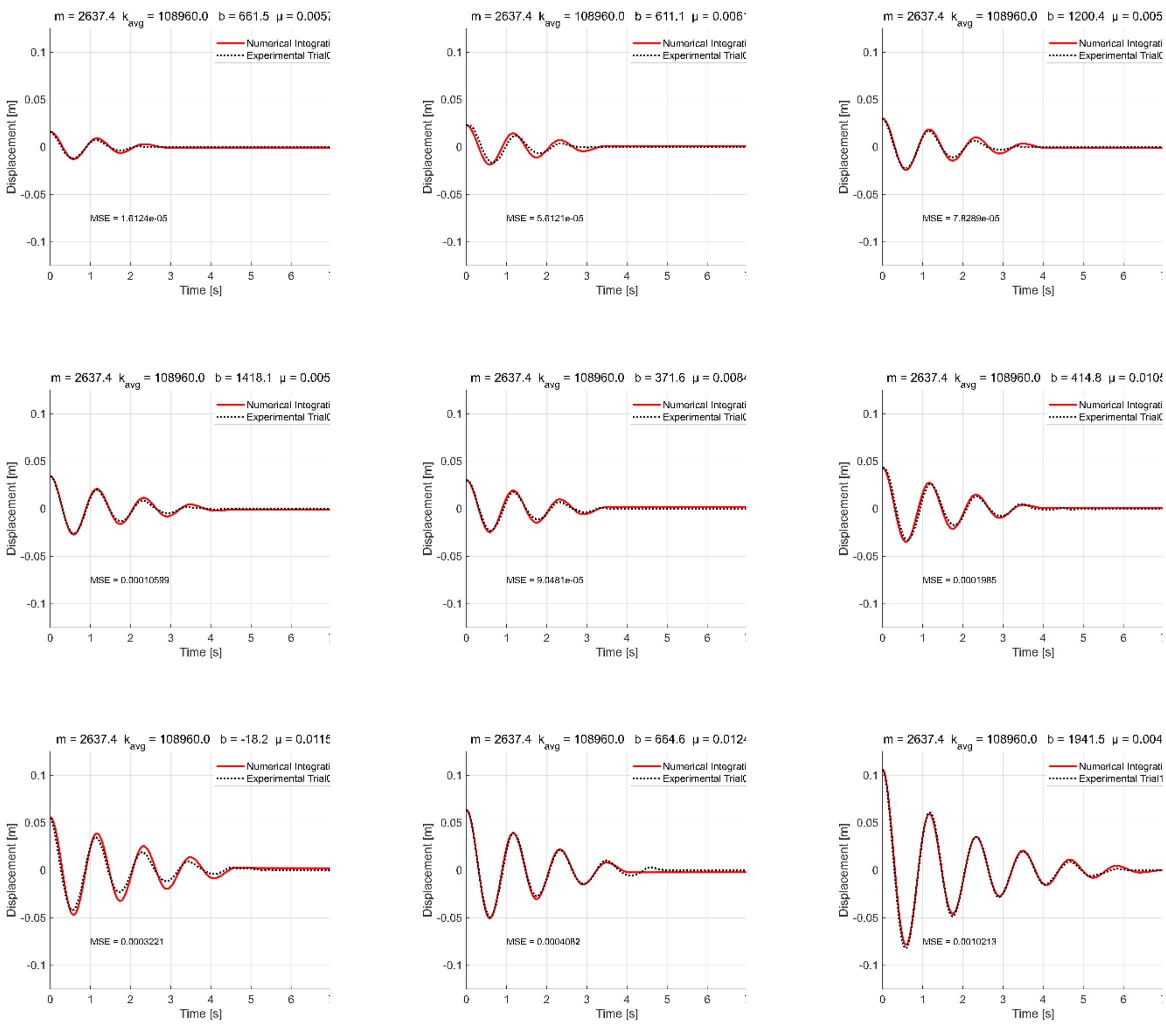

Figure 12. Prediction of displacement based on EOM and numerical integration for long-spring case and all initial displacements at water level of H=2.36m.

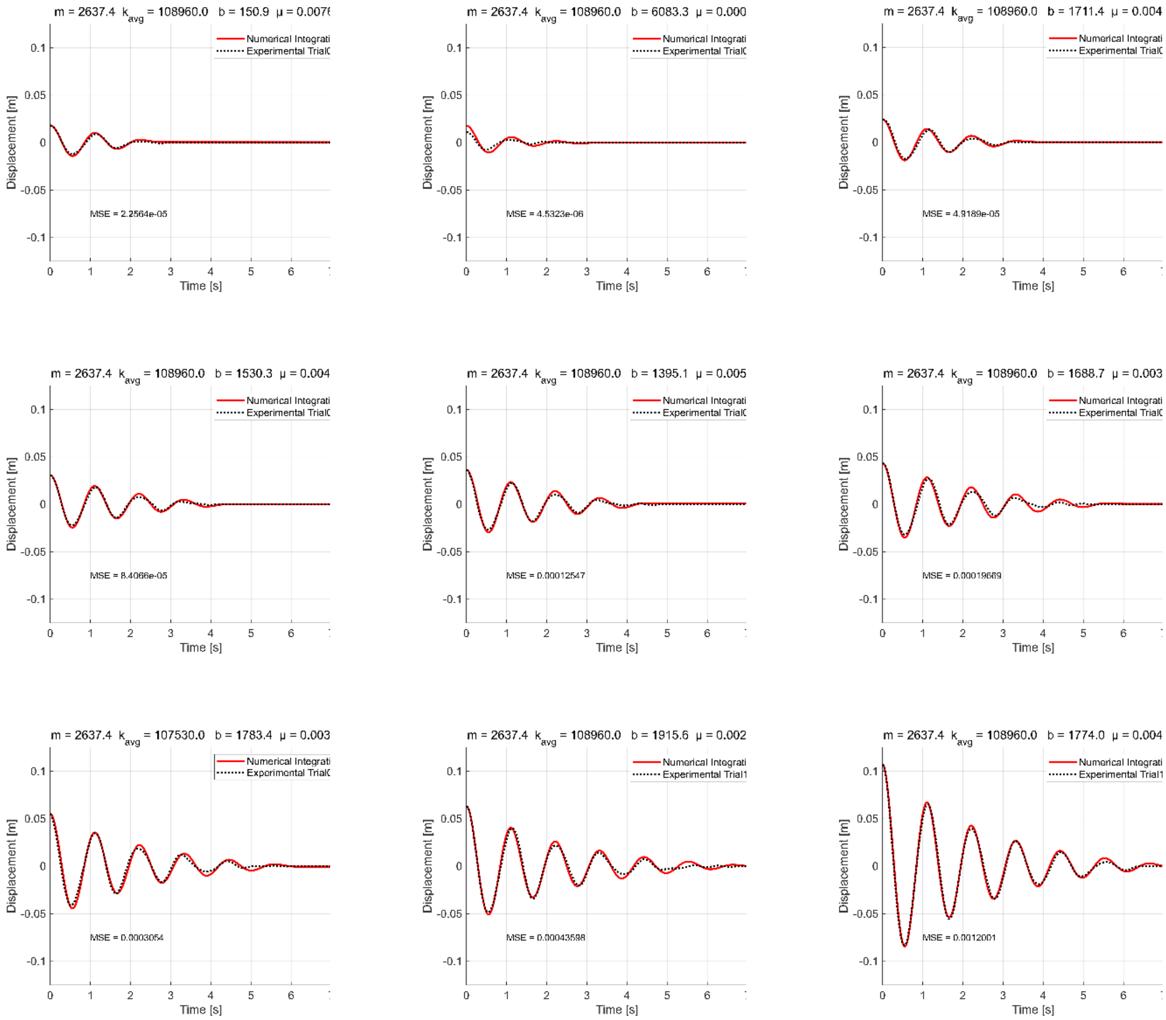

Figure 13. Prediction of displacement based on EOM and numerical integration for long-spring case and all initial displacements at water level of H=2.29m.

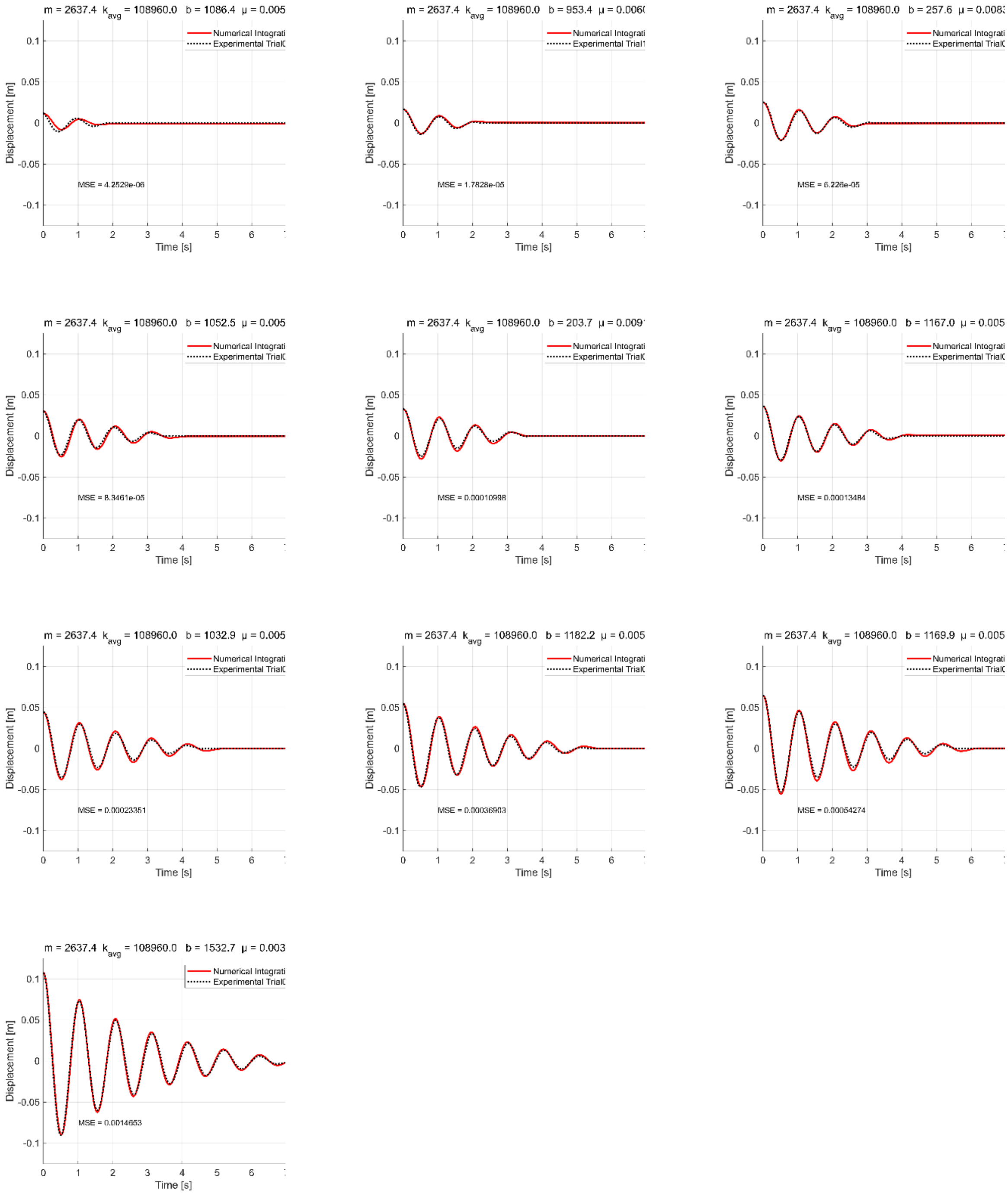

Figure 14. Prediction of displacement based on EOM and numerical integration for long-spring case and all initial displacements at water level of H=2.22m.

The same optimization procedure was applied to the short-spring configuration to determine the corresponding added mass and drag coefficients under each submergence level. The results for the largest initial displacement are summarized in Table 6. These values follow trends similar to those observed in the long-spring case, though the magnitude of the drag coefficient is generally higher owing to the increased stiffness and resulting higher oscillation frequencies. The predicted time-history responses for the short-spring case with these parameters for full submergence levels is shown in Figs. 15 and 16 and shows good correlation with the measured response.

Table 6. Parameters calculated from Method 1 for short-spring case with largest initial displacement at different water levels.

Submergence H [m]	m_a [kg]	C_d [-]	Mass of water in cells [kg]	Initial Disp. [m]
2.22	0	7.98	300	0.033
2.29	0	4.98	669	0.033
2.36	299	8.00	1015	0.033
2.43	1056	9.71	1104	0.033
2.57	1079	10.10	1104	0.033

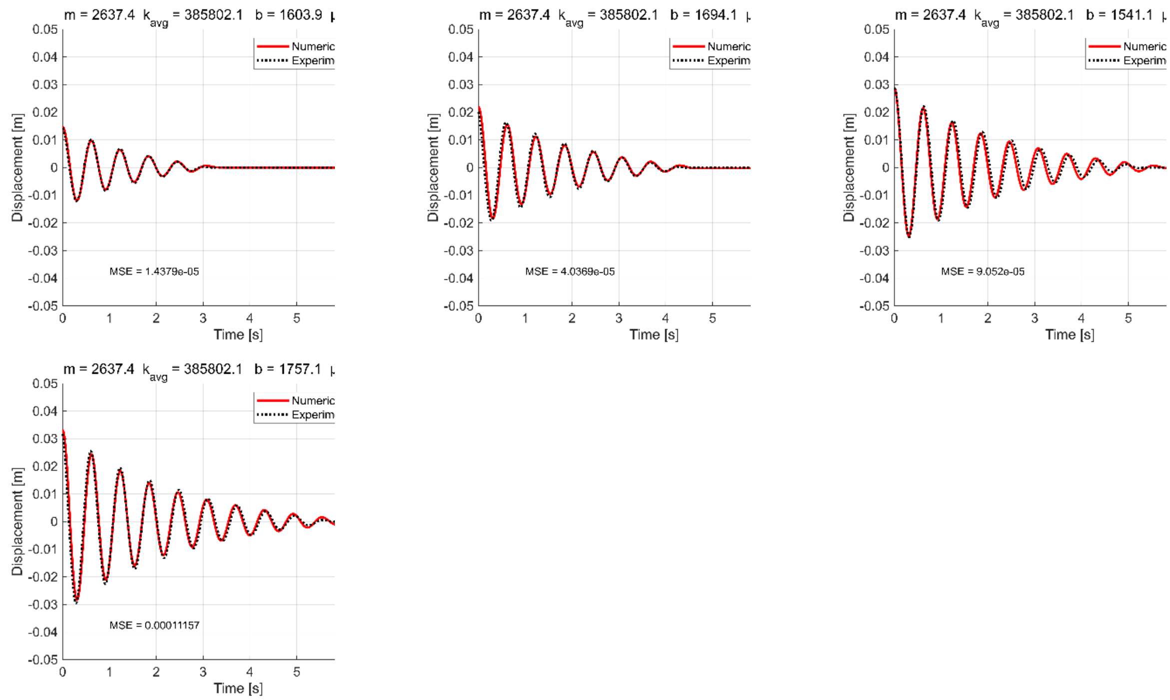

Figure 15. Prediction of displacement based on EOM and numerical integration for short-spring case and all initial displacements at water depth of H=2.57m.

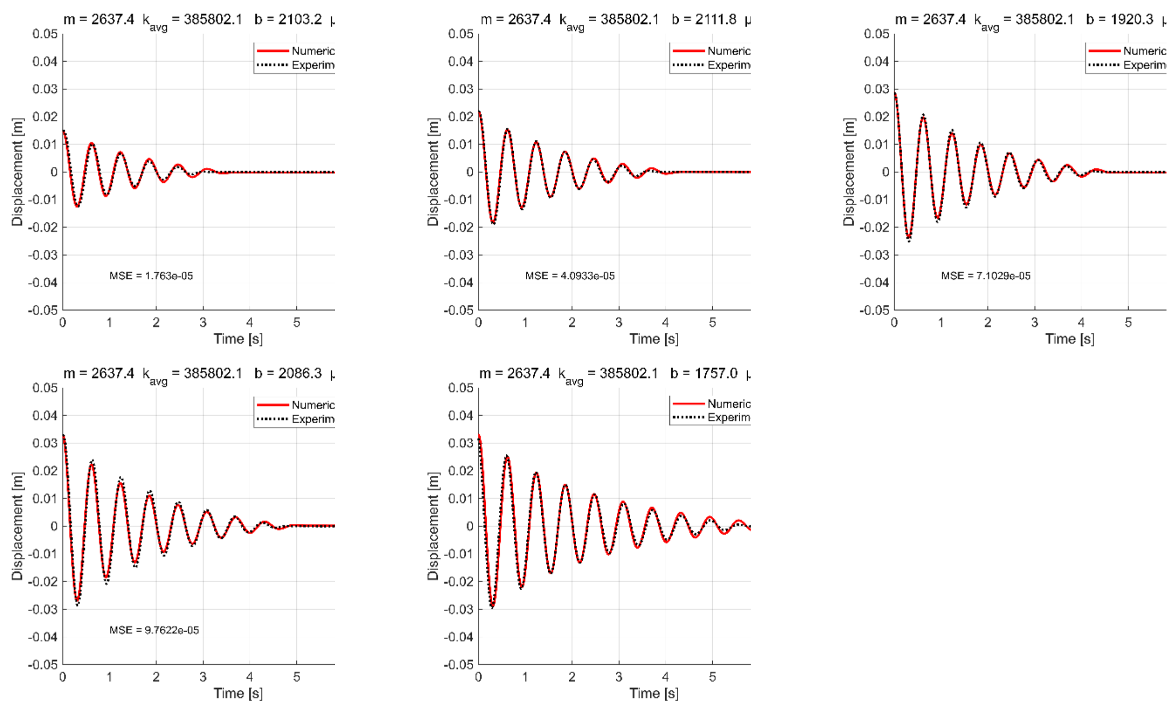

Figure 16. Prediction of displacement based on EOM and numerical integration for short-spring case and all initial displacements at water depth of H=2.43m.

The numerical solution for the short-spring case at a submergence level of H = 2.36 m exhibits modulation effects in the experimental response that are not captured by the simplified equation of motion as seen in Fig. 17. These amplitude fluctuations and phase shifts suggest the influence of complex fluid–structure interactions, likely due to sloshing of water entrapped between the bridge webs and justify this speculation later. The simplified hydrodynamic model does not incorporate these internal fluid dynamics, which explains the deviation between measured and predicted responses.

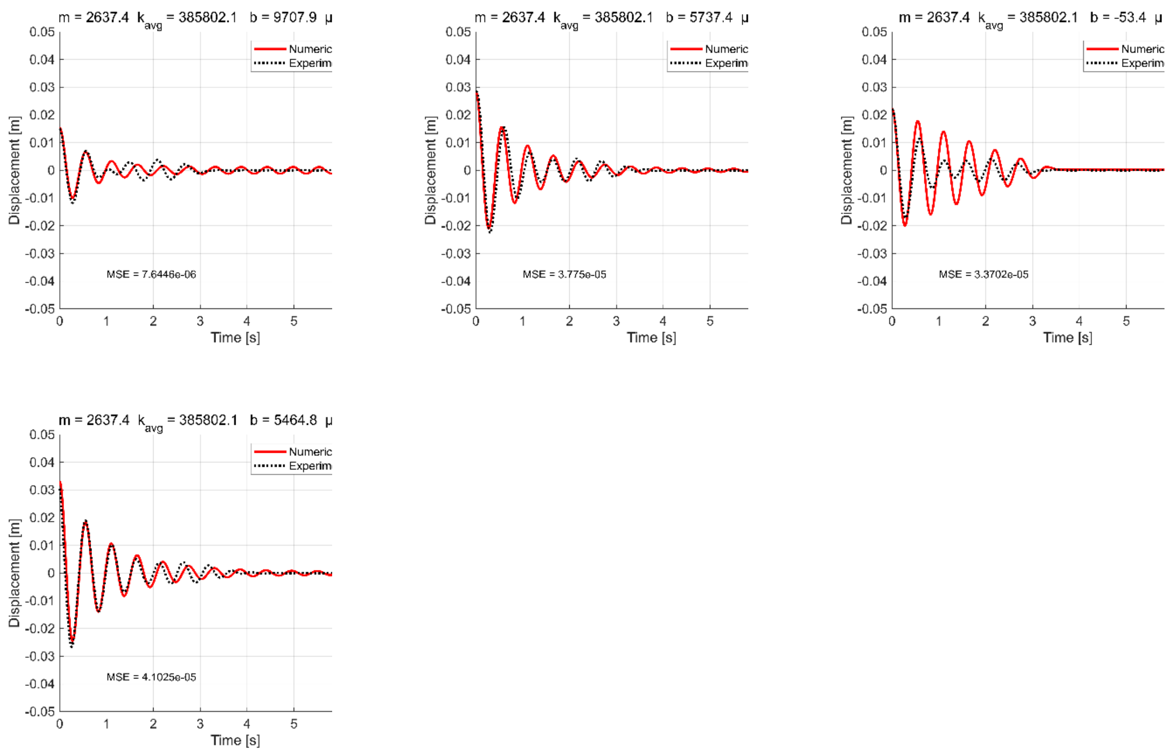

Figure 17. Prediction of displacement based on EOM and numerical integration for short-spring case and all initial displacements at water depth of H=2.36m.

A similar modulation pattern is observed for the submergence level H = 2.29 m, where the onset of amplitude modulation coincides with a noticeable phase shift in the displacement response as seen in Fig. 18. These behaviors cannot be reproduced using the current EOM formulation and are likely associated with transient water motion opposing the structural vibration. Both load cell and string potentiometer data confirm the presence of this dynamic interaction.

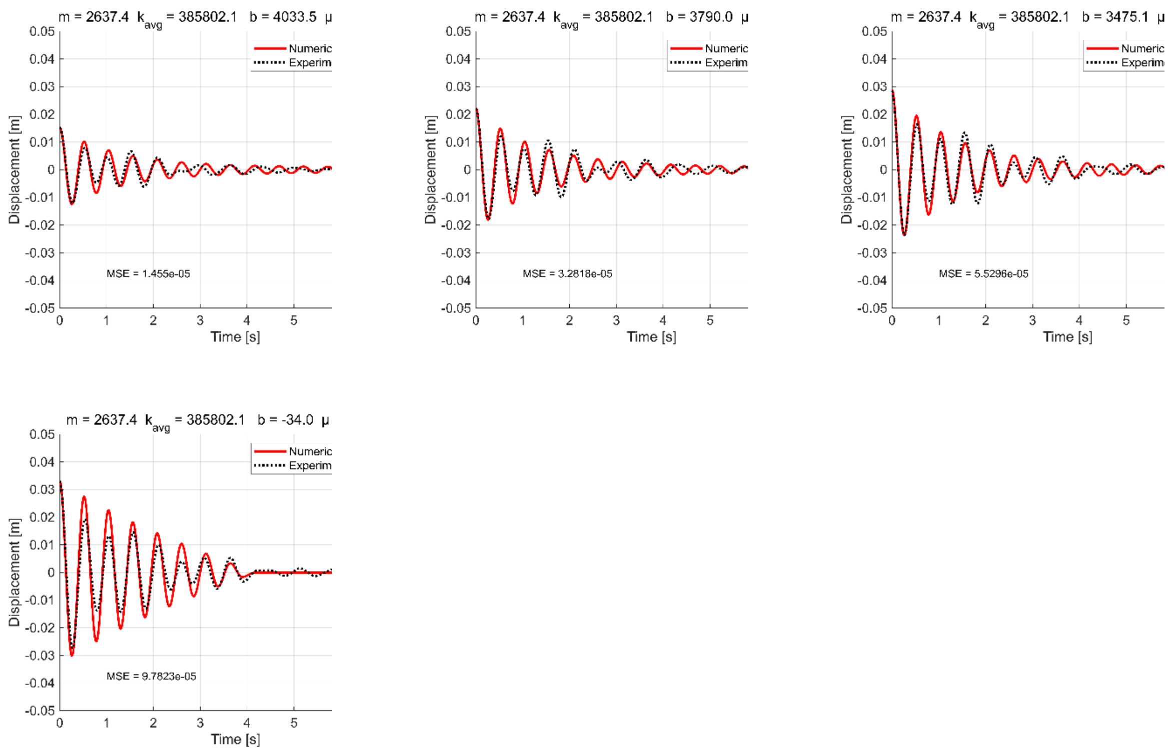

Figure 18. Prediction of displacement based on EOM and numerical integration for short-spring case and all initial displacements at water depth of H=2.29m.

At the minimum submergence level of H = 2.22 m, the modulation effects are less pronounced, indicating weaker fluid coupling. Although small fluctuations in amplitude remain visible, the dominant oscillatory frequency is largely unaffected, suggesting that sloshing-related interactions diminish as the water depth approaches the lower bound of structural engagement.

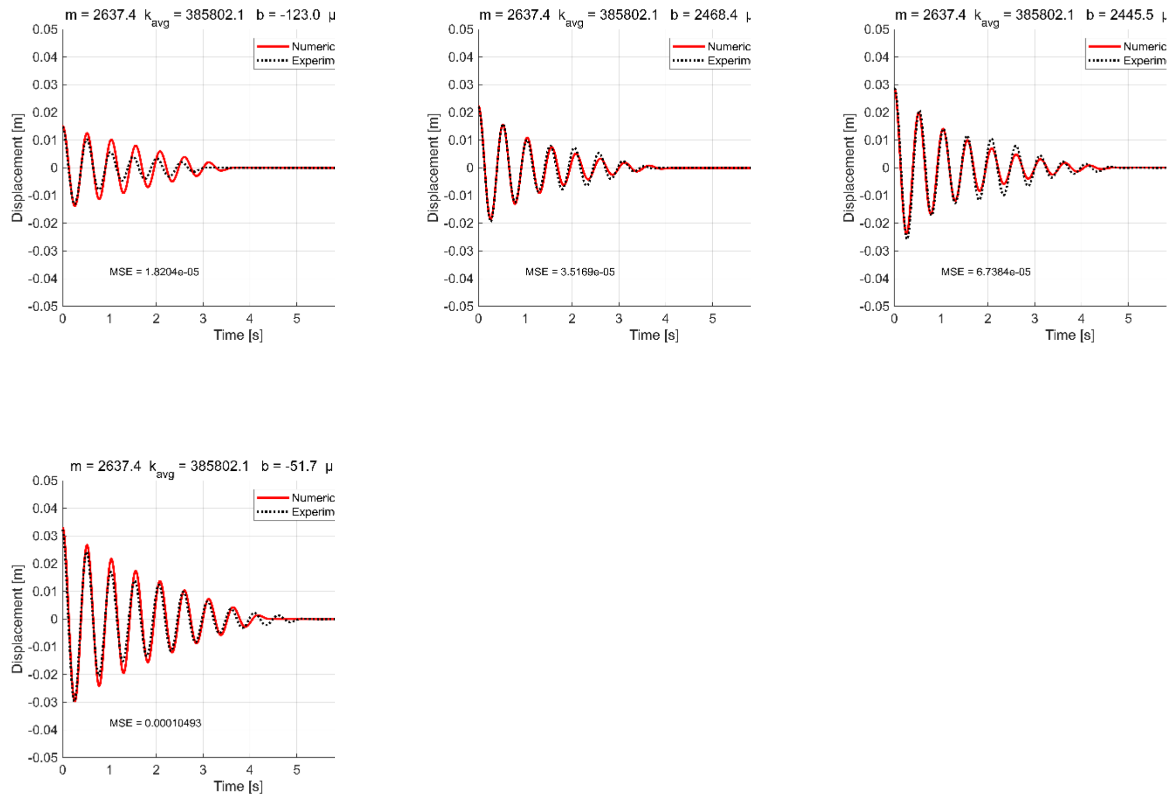

Figure 19. Prediction of displacement based on EOM and numerical integration for short-spring case and all initial displacements at water depth of H=2.22m.

Method 2 – CH Instant Method

The second approach used to estimate the added mass and drag coefficients evaluates the equation of motion at specific critical instants in the time-history response. This method is called the CH Instant Method in this report and isolates the contribution of individual force components by selecting instants in the time-history response when certain terms in the equation of motion are zero. This allows direct computation of either the added mass or the drag coefficient without relying on full time-series fitting. The method provides an independent check on the parameters obtained through optimization and offers physical insight into the dominant hydrodynamic mechanisms.

Added mass was determined at the instant of maximum acceleration, which coincides with zero velocity. Under this condition, the drag force is zero and the friction contribution is constant, reducing the equation of motion to a balance between structural mass, added mass, stiffness, and measured acceleration. Evaluating the equation of motion at this instant allows direct computation of the added mass using the known stiffness, measured displacement, and recorded acceleration.

$$m\ddot{x} + c\dot{x} + kx + sign(\dot{x})\mu_f(mg - \forall\rho_w g) + m_a\ddot{x} + \frac{1}{2}\mathrm{C_d}\ \rho_\mathrm{w}\ \mathrm{A}\dot{x}|\dot{x}| = 0 \qquad \text{[Eq. 17]}$$

When $\ddot{x}$ is maximum, $\dot{x}$ is 0 so, at the instant of maximum $\ddot{x}$ the EOM becomes:

$$kx = m\ddot{x} + m_a\ddot{x} \qquad \text{[Eq. 18]}$$

$$m_a = \frac{(-kx - m\ddot{x})}{\ddot{x}} \qquad \text{[Eq. 19]}$$

The drag coefficient was estimated at the instant when displacement crosses zero, an instance that is characterized by maximum velocity and zero acceleration. At this point, the inertial terms vanish, and the equation of motion simplifies to an expression governed solely by velocity-dependent forces, namely viscous damping, friction, and hydrodynamic drag. This enables an explicit calculation of the drag coefficient based on the measured velocity and known damping and friction parameters. Although the exact timing of the true velocity peak may differ slightly from the zero-crossing, the approximation is sufficiently accurate for the purposes of this analysis.

When $\dot{x}$ is maximum, $\ddot{x}, x$ are both 0 so, at the instant of maximum $\dot{x}$ the EOM becomes:

$$c\dot{x} + sign(\dot{x})\mu_f(mg - \forall\rho_w) + \frac{1}{2}\mathrm{C_d}\ \rho_\mathrm{w}\ \mathrm{A}\dot{x}|\dot{x}| = 0 \qquad \text{[Eq. 20]}$$

where the values of m, $\forall, \rho_w$, c, A are known along with the measured displacement and acceleration, the drag coefficient can be obtained from the rearranged equation of motion as:

$$\mathrm{C_d} = -2\frac{sign(\dot{x})\mu_f(-\forall_s\rho_w+mg)+c\dot{x}}{\rho_w A\dot{x}|\dot{x}|} \quad \text{[Eq. 21]}$$

To apply the CH Instant Method, the acceleration time-history measured at the deck from sensor *Accel1x* was first low-pass filtered and detrended to reduce noise and drift. Velocity was then computed by numerically integrating the filtered acceleration using the trapezoidal rule at a time step of 0.001s. The added mass was evaluated at the instant of maximum acceleration (where velocity is zero), while the drag coefficient was determined at the first zero-crossing of displacement (where acceleration is zero and velocity is maximum). The damping ratio, friction coefficient, and stiffness were fixed at their mean dry-test values to isolate the hydrodynamic contributions.

This method provides a robust estimate of the added mass because the initial acceleration peak is well defined and relatively insensitive to measurement noise. In contrast, the drag coefficient is more sensitive to uncertainty because it depends on velocity, which is obtained through numerical integration and therefore amplifies filtering and noise effects. Nevertheless, the method produces consistent trends and serves as an important independent comparison to the optimization-based results. In this approach, the displacement signal is also approximated using a trigonometric function, which provides a smooth representation of the motion and enables accurate identification of peak acceleration and zero-crossing instants required for evaluating the added mass and drag terms.

Table 7. Parameters calculated using CH Instant Method for long-spring case with water level of H=2.57m.

Potential Energy [kN-m] [kJ]	Added Mass [kg]	Cd [-]
63	975	48.9
133	1077	30.6
195	1125	24.7
249	1132	23.0
174	1084	27.00
374	1147	18.8
591	1174	13.7
790	1185	12.5
2280	1232	8.1

Table 8. Parameters calculated using CH Instant Method for short-spring case with water level of H=2.57m.

Potential Energy [kN-m] [kJ]	Added Mass [kg]	Cd [-]
40	858	44.5
76	946	21.8
159	1014	14.1
216	1030	13.1

Discussion

Added Mass

The results obtained from both the optimization procedure (Method 1) and the CH Instant Method (Method 2) enable a comprehensive assessment of the hydrodynamic effects acting on the bridge during submerged free-vibration response. By comparing the estimated added mass and drag coefficients across multiple submergence levels and initial displacements, clear behavioral trends emerge that provide insight into the governing fluid–structure interaction mechanisms.

Figure 20 illustrates the variation of added mass for all tests conducted at a water depth of $H = 2.57$ m. The results show that added mass remains relatively constant across different levels of initial displacement. This behavior aligns with physical expectations, as added mass is primarily governed by the geometry of the submerged structure and the surrounding fluid domain, rather than by the amplitude of motion. The agreement between Method 1 and Method 2 further validates the stability and reliability of the added mass estimation.

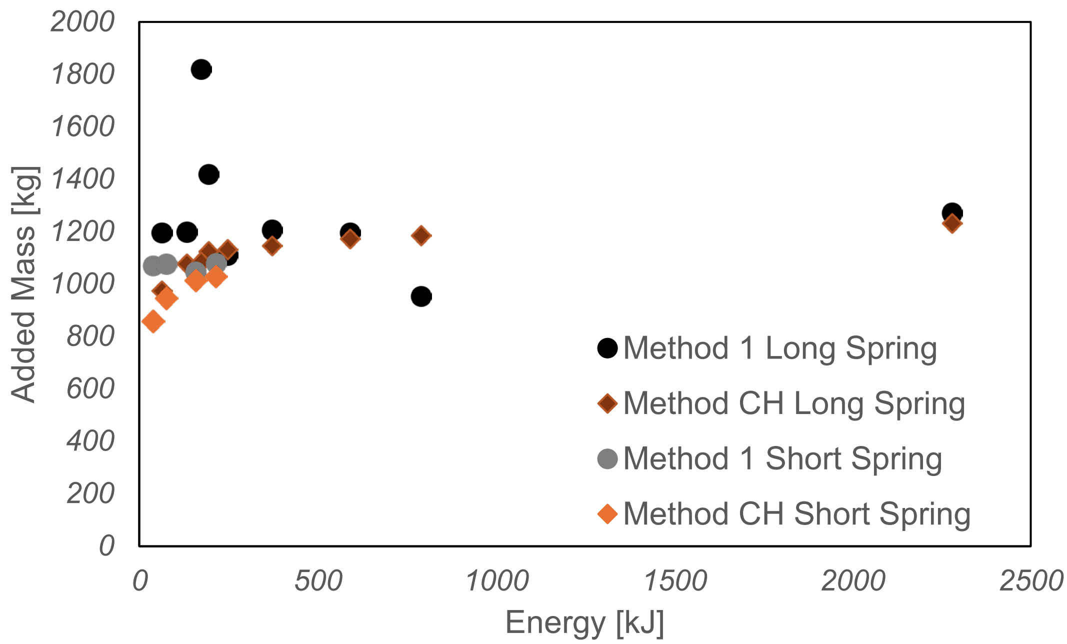

Figure 20. Added mass for all cases with H=2.57m submergence.

Drag Coefficient

Figure 21 shows the corresponding drag coefficients for the same set of submerged trials. Unlike added mass, the drag coefficient exhibits a strong dependence on the initial displacement amplitude, generally decreasing as displacement increases. This reduction suggests that the damping effect of the fluid is less significant at higher velocities, which is consistent with known nonlinear drag behavior under impulsive and transient flow conditions. Although the CH Method produces drag estimates that are higher than typical steady-flow values, the observed trend remains consistent across both approaches.

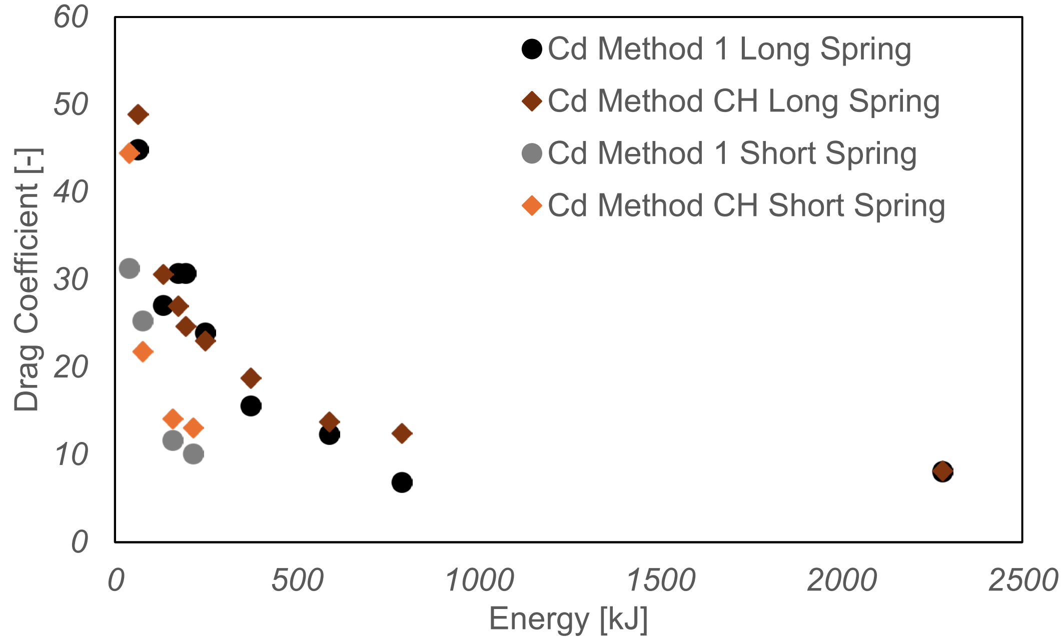

Figure 21. Drag coefficients for all cases with H=2.57m submergence.

It is important to note that classical drag coefficients for steady flow conditions are typically of order unity. However, the snap-test loading generates rapid, impulsive motion characterized by unsteady flow separation, added-mass interaction, and transient vortex formation. Under such conditions, the quasi-steady drag formulation used herein does not fully represent the underlying physics, and the elevated values of $C_d$reflect the strongly unsteady nature of the event rather than the steady-flow resistance typically assumed in hydrodynamic analyses.

Case for constant values of C_d and m_a

To further examine the predictive capability of the model, constant values of added mass and drag coefficient derived from the fully submerged case were applied to all initial displacement levels. These parameters were combined with the mean damping ratio, friction coefficient, and stiffness values obtained from the dry tests. Table 9 summarizes the constant values used. This approach serves to evaluate how well a simplified, displacement-independent parameter set can reproduce the system response across a range of initial energies.

Table 9. Constant values used for long-spring case at fully-submerged conditions with water level of H=2.57m.

ζ [−]	0.0174
Damping [N s/m]	590
Friction Coefficient [-]	0.0073
Added Mass [kg]	2042
Drag Coefficient [-]	25

The constant hydrodynamic properties used in the numerical solution of the equation of motion (Eq. 15) reproduce the general behavior of the system but begin to lose accuracy after the first two vibration cycles, particularly in terms of phase alignment and amplitude decay. This limitation is expected given the simplicity of the constant-parameter assumption. To improve the prediction, the same response was re-evaluated using the added mass and drag coefficients obtained from Method 1, while maintaining the average dry-test values for damping and friction. In this formulation, the added mass and drag correspond specifically to the fully submerged case and the largest initial displacement. The resulting predictions show a marked improvement, with better agreement in both amplitude and phase throughout the entire response for the short-spring case. The corresponding displacement histories are presented in Figure 22.

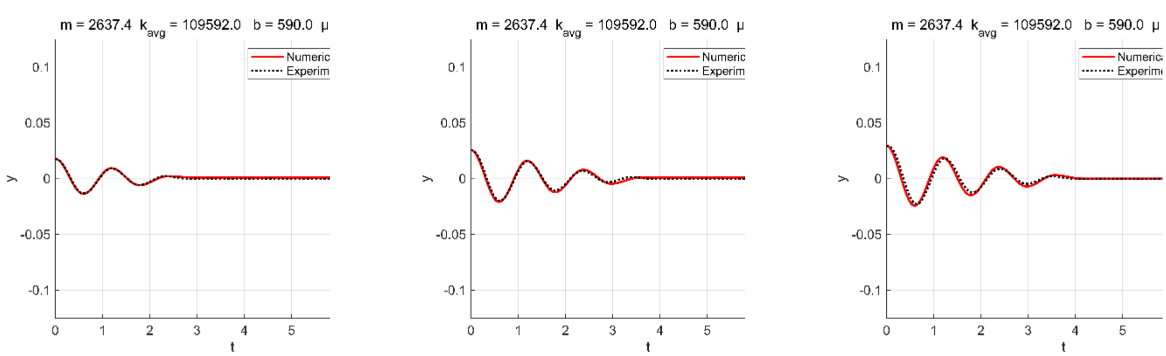

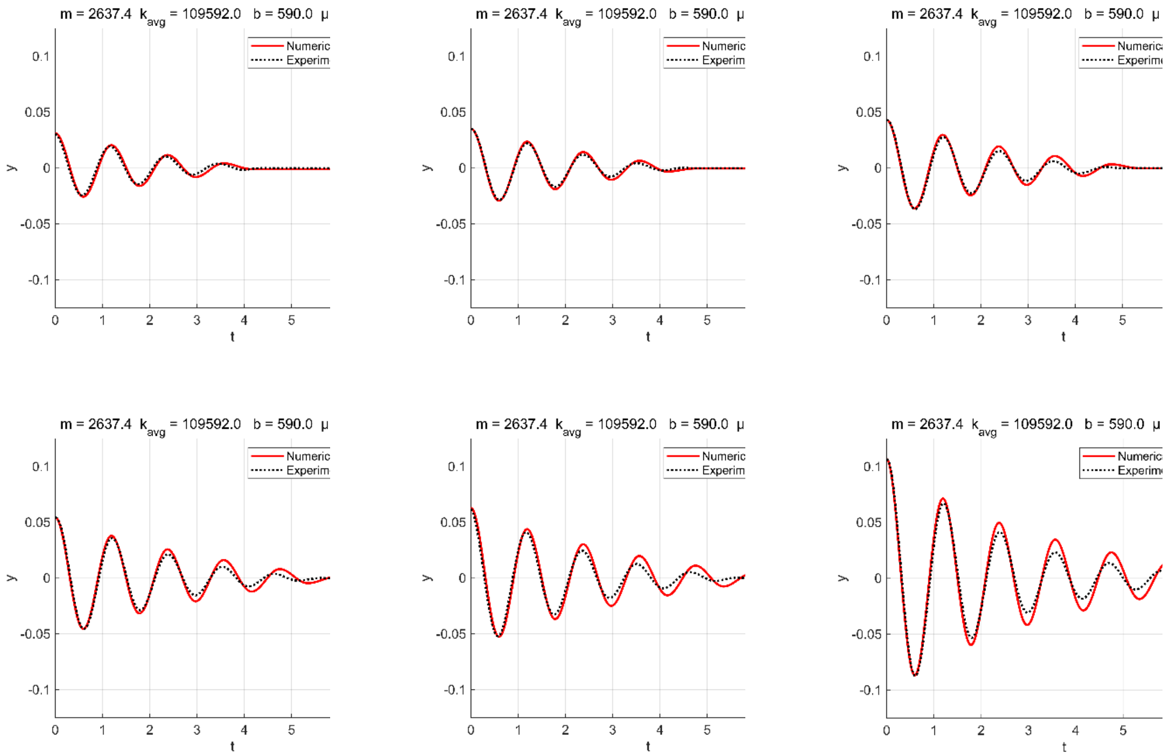

Figure 22. Prediction of displacement history based on EOM and numerical integration for short-spring case and all initial displacements with water level of H=2.57m.

Fully Submerged Case Analysis of Results

The results for the long-spring configuration at full submergence ($H = 2.57$ m) are shown in Figure 23 and summarized in Table 10. A clear distinction emerges in the relative magnitudes of the hydrodynamic terms: the added mass contribution is consistently an order of magnitude larger than the drag force. This disparity indicates that the system's response is governed primarily by inertial hydrodynamic effects, with drag playing a secondary role for the motion imposed here. As a result, the added mass term exerts the dominant influence on the oscillatory behavior under fully submerged conditions.

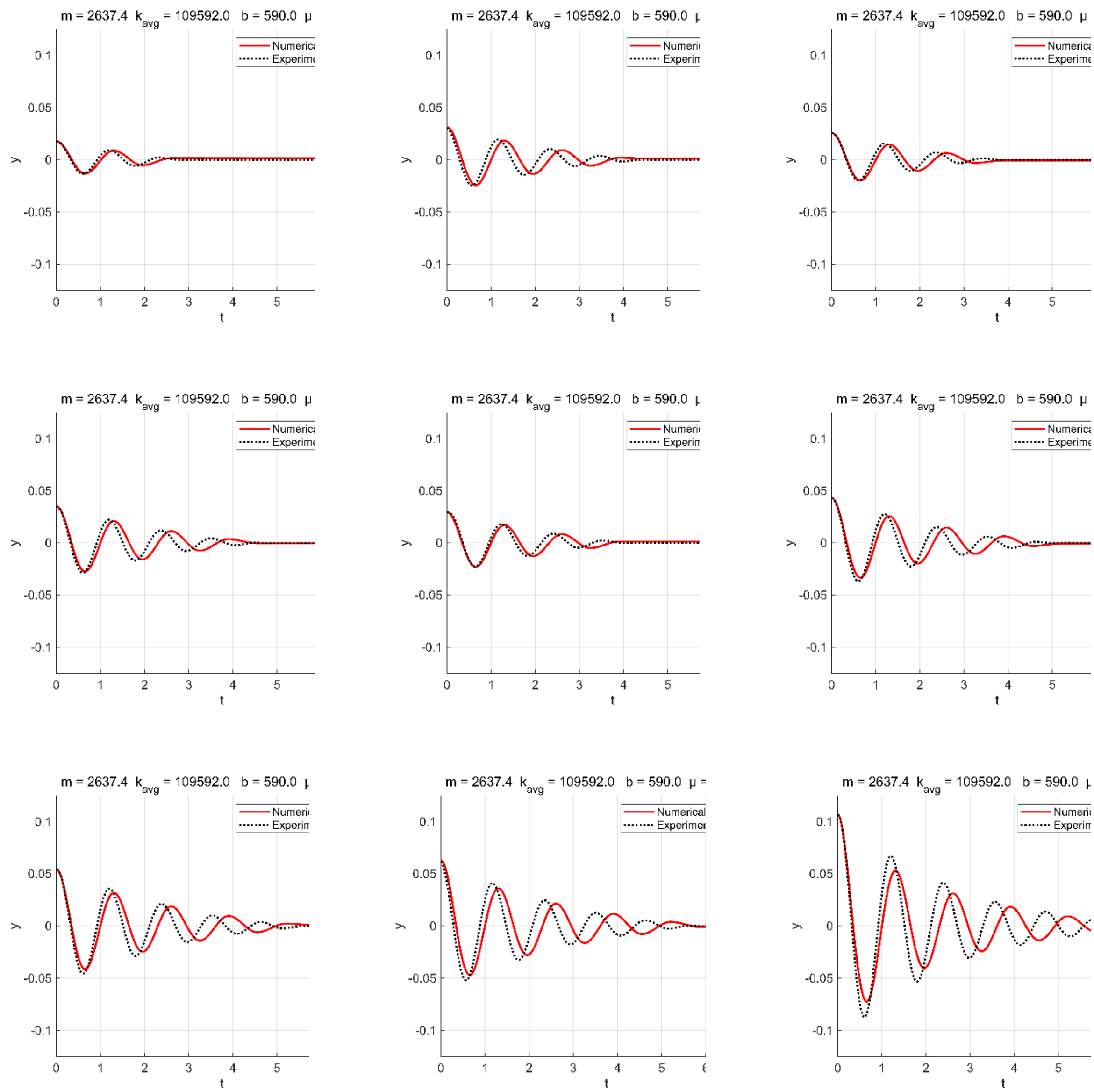

Figure 23. Prediction of displacement history based on the equation of motion (Eq. 15) and numerical integration for long-spring case and all initial displacements with water level of H=2.57m.

Table 10. Summary of results for long-spring case at fully submerged water level of H=2.57m.

$x_0\ [m]$	$c_d[-]$	$m_a\ [kg]$	$m\ [kg]$	$\left.\frac{du}{dt}\right\|_{max}$	$(m+m_a)\left.\frac{du}{dt}\right\|_{max}$	U_{max}	$A\ [m^2]$	$\rho_w \left[\frac{\mathrm{kg}}{\mathrm{m}^3}\right]$	$\frac{1}{2} C_d \rho_w A U_{max}^2$
0.0178	69.1	1271.4	2637.4	0.424	1657	0.061	0.97	1000	124

0.0258	34.5	1271.4	2637.4	0.627	2452	0.098	0.97	1000	159
0.0312	24.6	1271.4	2637.4	0.763	2983	0.122	0.97	1000	177
0.0352	20.0	1271.4	2637.4	0.863	3373	0.140	0.97	1000	189
0.0295	27.1	1271.4	2637.4	0.720	2816	0.114	0.97	1000	172
0.0432	14.3	1271.4	2637.4	1.057	4130	0.174	0.97	1000	210
0.0543	9.9	1271.4	2637.4	1.322	5166	0.221	0.97	1000	235
0.0628	8.0	1271.4	2637.4	1.519	5936	0.255	0.97	1000	252
0.1067	3.8	1271.4	2637.4	2.476	9678	0.418	0.97	1000	323

SUMMARY AND CONCLUSIONS

This study investigated the hydrodynamic response of a bridge superstructure model subjected to lateral motions under varying levels of water submergence. Experiments were conducted using a 1:5 scaled prestressed girder bridge model installed in the Long Wave Flume at the O. H. Hinsdale Wave Research Laboratory. Snap-release tests were performed under both dry and submerged conditions using two spring configurations that represent different structural lateral stiffness values. The resulting free-vibration responses were used to determine mechanical properties of the bridge and support system and to quantify hydrodynamic added mass and drag forces associated with submerged and partially submerged motions.

Dry-condition tests established baseline mechanical parameters for the bridge, spring, and rail system. Measured stiffness values were approximately 109 kN/m for the long-spring configuration and 404 kN/m for the short-spring configuration, with average damping ratios of 0.017 and 0.013, respectively. Friction coefficients associated with the linear sliding bearings were on the order of 0.006 to 0.007. These parameters were subsequently treated as fixed mechanical properties in the analysis of submerged tests.

Submerged experiments were conducted over a range of water depths, from minimal submergence to full submergence of the bridge cross section. Hydrodynamic added mass and drag coefficients were estimated using two complementary approaches: numerical optimization of the governing equation of motion and an instantaneous method whereby certain dynamic properties are maximized (or vanish) at specific instances in the time history. Both approaches produced consistent trends in the estimated hydrodynamic parameters.

Results indicate that added mass remains approximately constant for a given level of submergence and is largely independent of excitation amplitude. For the fully submerged condition, added mass values were typically 1000 to 1300 kg, representing a substantial fraction of the structural mass of the bridge model. In contrast, the effective drag coefficient decreases with increasing oscillation amplitude, reflecting the highly unsteady flow conditions generated during snap-release motion.

The results also show that hydrodynamic inertial forces dominate the submerged response of the bridge model. Under fully submerged conditions, the contribution of added mass to the governing equation of motion was approximately an order of magnitude larger than the drag contribution. Consequently, bridge response during impulsive loading events is controlled primarily by fluid inertia rather than viscous resistance.

For partially submerged conditions, the measured response exhibited amplitude modulation and phase shifts not captured by the simplified hydrodynamic model. These effects are likely associated with sloshing of water trapped between girders, introducing an additional fluid-structure interaction mechanism that are not represented in the present equation-of-motion formulation.

Overall, the experimental results provide insight into the hydrodynamic forces acting on bridge structures subjected to dynamic loading conditions in submerged environments. The findings highlight the dominant role of added mass and demonstrate that drag forces associated with rapid transient motion differ significantly from steady-flow assumptions commonly used in bridge hydrodynamic loading models.

The results of this study provide experimentally derived hydrodynamic parameters that can be used to improve analytical and numerical models of bridge response under hydraulic loading conditions. In particular, the measured added mass and drag characteristics provide a basis for calibrating simplified fluid-structure interaction models used in bridge dynamic analyses and coastal hazard assessments. The findings also highlight the importance of accounting for hydrodynamic inertial effects when evaluating bridge response during impulsive loading events such as tsunami-induced flows, wave impacts, or debris interaction. The experimental dataset developed in this study can serve as a benchmark for validating computational models, including Smoothed Particle Hydrodynamics (SPH) simulations and other numerical approaches used to simulate wave-structure interactions. Future work should focus on improved characterization of partially submerged conditions, particularly the influence of water sloshing within girder lines and other geometric features that may introduce additional fluid-structure interaction effects not captured by simplified hydrodynamic formulations.

Taken together, the findings of this study provide an experimental basis for improving hydrodynamic models for bridge structures and contributes to development of more robust analytical and numerical tools to evaluate bridge performance under extreme coastal and hydraulic loading events.

DATA AVAILABILITY STATEMENT

All electrochemical and structural response data that support the findings of this study are in the Zenodo Data Share repository with the identifier https://zenodo.org/records/18989892

REFERENCES

Blevins, R. D. (1990). Flow-Induced Vibration, 2nd Ed., Van Nostrand Reinhold, New York, 477 pp., ISBN 0-442-23913-7

Bradner, C., Schumacher, T., Cox, D. T., and Higgins, C. (2010). "Experimental setup for a large-scale bridge superstructure model subjected to waves," ASCE J. of Waterway, Port, Coastal, and Ocean Engineering, 137(1), pp. 3–11.

Dean, R. G., and Dalrymple, R. A. (1991). Water Wave Mechanics for Engineers and Scientists, Advanced Series on Ocean Engineering, Vol. 2, World Scientific Publishing, Singapore, 368 pp. ISBN 981-02-0420-5.

Guo, A. and Fang, Q. and Bai, X. and H. Li, (2015). "Hydrodynamic experiment of the wave force acting on the superstructures of coastal bridges," ASCE J. Bridge Engineering, 20 (12).

Istrati, D., and I. Buckle, (2014). "Effect of Fluid–Structure Interaction on Connection Forces in Bridges Due to Tsunami Loads," Proceedings of the 30th U.S.-Japan Bridge Engineering Workshop, Washington, DC.

Morison, J. R., O'Brien, M. P., Johnson, J. W., and S.A. Schaaf, (1950). "The force exerted by surface waves on piles," Petroleum Trans., AIME, 189, 149–154.

Robertson, I. N., Riggs, H. R., Yim, S. C. S., and Y.L. Young, (2007). "Lessons from Hurricane Katrina Storm Surge on Bridges and Buildings," ASCE J. of Waterway, Port, Coastal, and Ocean Engineering, ASCE, 133(6), 463–483. DOI: 10.1061/(ASCE)0733-950X(2007)133:6(463).

Yeh, H., Robertson, I., and J. Preuss, (2013). "Tsunami forces on bridges," ASCE J. of Waterway, Port, Coastal, and Ocean Engineering, 139(3), 163–172.